Microbeam-Radiation-Therapy (MRT): Characterizing a Novel MRT Device Using High Resolution 3D Dosimetry

by

Qiongge Li

Department of Medical Physics
Duke University

Date:_____

Approved:

_____
Mark Oldham, Supervisor

_____
Fangfang Yin

_____
James MacFall

Thesis/Dissertation submitted in partial fulfillment of
the requirements for the degree of
Master of Science in the Department of
Medical Physics in the Graduate School
of Duke University

2014

ABSTRACT

Microbeam-Radiation-Therapy (MRT): Characterizing a Novel MRT Device Using High Resolution 3D Dosimetry

by

Qiongge Li

Department of Medical Physics
Duke University

Date:_____
Approved:

_____
Mark Oldham, Supervisor

_____
Fangfang Yin

_____
James MacFall

An abstract of a thesis submitted in partial fulfillment of the requirements for the degree of Master of Science in the Department of Medical Physics in the Graduate School of Duke University

2014

Abstract

Purpose:

The feasibility of MRT has recently been demonstrated utilizing a new technology of Carbon-Nano-Tube (CNT) field emission x-ray sources. This approach can deliver very high dose (10's of Gy at a nominal dose rate of 1.16 Gy/min) in narrow strips (sub-mm) of radiation, which enables the study of novel radiation treatment approaches. Here we investigate the application of high- resolution (50*um* isotropic) PRESAGE®/Optical-CT 3D dosimetry techniques to characterize the radiation delivered in this extremely challenging scenario.

Methods:

The CNT field emission x-ray source irradiator comprises of a linear cathode array and a novel collimating system. The device delivers small 'strip' beams, with nominal dimension (at the isocenter) of 65mm x 300um, at an energy of 160 kVp. To characterize the MRT beams, an ultra-high-resolution prototype 3D dosimetry system was constructed and optimized, consisting of two parts: a radiochromic 3D dosimetry material PRESAGE, and a high resolution small field-of-view optical-CT imaging system for dose-readout (DMicrOS – Duke Micro Optical-CT Scanner). Small PRESAGE cylindrical dosimeters were irradiated by CNT MRT delivering 3 strips of radiation with a nominal entrance dose of 32 Gy and 16 Gy, Other similar dosimeters were irradiated to

doses of between 16-32Gy with a regular x-ray irradiator collimated to microscopic strip-beams using a customized cerrobend collimator. Fifty *um* (isotropic) 3D dosimetry was performed on all dosimeters using the DMicrOS (including a stray light deconvolution correction). The Percentage Depth Dose (PDD), Peak-to-Valley Dose Ratio (PVDR) and beam width (FWHM) data were obtained and analyzed. Independent verification using EBT2 radiochromic film was performed in select cases.

Results:

Basic testing of the DMicrOS system indicated this system's performance: Signal-to-Noise-Ratio (SNR) for a flood count image is 46.6; The dark noise level for count image is 3.8 (mean: 3.8, sigma: 0.04); The dynamic range was 3800 counts, spatial resolution limit is 29.6 micron in object space, Field-Of-View (FOV) is specified to 47.6 mm (HFOV) x 35.8 mm (VFOV). Additionally, a Modulation-Transfer-Function (MTF) was generated from stray light correction experiment. When applied to the PRESAGE dosimeters irradiated with MRT strip beams, high-resolution 3D images were successfully achieved with the prototype system, enabling extraction of dose profiles. The PDDs for both Multi-beam irradiation and three strips irradiation showed steep dose falloff with the depth, which suggests a weak penetration (PDD drops to 39.5% at depth of 14mm for multi-beam case and drops to 86.5% at the depth of 14 mm for three strips). The small variation between different beams' widths/spacings as well as their small variation at different depth in CNT MRT system suggested the effectiveness of its novel collimating

system. Moreover, a smaller beams' widths/spacings have been achieved by CNT irradiator than the multi-beam irradiator. Beam spacing between the three strips has an average value of 0.9mm while that for the 13 strips is 1.5 mm at a depth of 16.5 mm. The average FWHM across all three beams remained constant (405.3um, sigma=13.2um) between depth of 3.0 ~14.0mm. Furthermore, the three strips show consistent PVDR values (the PVDR increased with depth from 6.3 at 3.0mm depth to 8.6 at 14.0mm depth).

Conclusion:

MRT dosimetry is extremely challenging due to the utilization of ultra-small field sizes and lower energy beams. Optical-CT micro 3D dosimetry is a promising approach, but achieving accurate, high quality data, at a resolution of ~50microns, remains non-trivial. The prototype ultra-high resolution optical-CT 3D dosimetry system introduced here, showed promise but to achieve 50micron 3D dosimetry requires exceptionally careful procedures especially regarding fluid handling and matching, precise dosimeter mounting, precise and robust mechanical motions (especially rotation), and stray-light artifact management. Further work is required to validate the accuracy of dose distribution and quantify the magnitude of artifacts as well as the efficacy of methods for their removal.

Contents

List of Tables

List of Figures

Acknowledgements

I would like to take this opportunity to express my profound gratitude and deep regards to my advisor Dr. Mark Oldham for his exemplary guidance, sincere help and constant encouragement throughout the course of this thesis. I also would like to acknowledge the support from Dr. Sha Chang for collaborative guidance and instruction, Titania Juang's direction and training and Steve Bache's efforts in implementing the PSF.

1. Introduction

According to the statistics released from American Cancer Society, a total of 1,665,540 new cancer cases and 585,720 cancer deaths are projected to occur in the United States in 2014. (Siegel et al. 2014) More than half of the cancer patients will receive radiation therapy as part of their cancer treatment. The goal for Radiation Therapy is to maximize the therapeutic ratio by delivering high dose to the tumor tissue while minimizing the damage to normal tissue. Conventional Radiation Therapy (such as Intensity Modulated RT or IMRT and 3D Conformal RT) is the current standard of care for many sites, and can achieve excellent target conformality (with uniform dose) and normal tissue sparing. However, there is still much room for improvement in cure and local control rates for many disease sites (such as gliosarcoma). Control rates can be increased through dose-escalation, but this is often not possible due to normal tissue toxicity limitations. Patients that fail and recur locally present another class of challenging clinical cases, where therapeutic re-treatment options are limited. In some of these scenarios Microbeam Radiation Therapy (MRT) may be a potential new treatment approach as described below.

1.1 Microbeam Radiation Therapy (MRT)

Microbeam Radiation Therapy (MRT) employs arrays of micro-planar thin beam, each with about 25 to 100 μm beam width and several hundreds of microns apart to precisely target the tumor tissue. (Hadsell, M. 2013)

MRT was first introduced by Laissue et al. in 1998 (Laissue et al. 1998[9]). Normal tissue from some rat experiments has been reported to be exceptionally resistant to dose (up to hundreds of gray) delivered by MRT. In contrast, MRT can significant delay tumor growth and cause tumor ablation. (Crosbie et al. 2010) Some preferential effect has been demonstrated for destroying the gliosarcoma vascular networks. (Bouchet et al. 2010) Although underlying radiobiological mechanisms at the cellular level are still unclear, the promising results from the previous investigation (i.e. evidences have been provided that MRT technique has successfully reduced tumor cell proliferation by 24 h post-irradiation(Crosbie, et al. 2010)) indicate the potential value of this radiotherapy technique. Therefore, an economical and handy MRT system, which can enable investigation of underlying biological mechanisms, would be valuable to develop.

1.1.1 Requirements for MRT System

Although MRT may have some advantages over traditional RT, it is relatively hard to achieve because of the following constraints:

The major constraint is that an orthovoltage energy level X ray source is required. Research has been reported that therapeutic effects are closely affected by variations in beam spacing and beam width. (Hadsell, M. 2013) Hence, preserving the shape of the X ray beams is essential to MRT effectiveness. Because of this, the X ray energy must not exceed a certain energy level, otherwise the secondary electrons will be scattered in

between the radiation planes and thus smear the dose distribution. Previous research has shown that the maximum energy that can be used in MRT is several hundred keV. (Hadsell, M. 2013)

Secondly, the MRT has to be delivered at a high dose rate. For even microscopic motion will affect the accuracy of beam width and beam spacing. Because of this strict immobilization requirement, a fast dose delivery is desired during MRT.

1.1.2 Limitations of Previous MRT Studies

Till today, only synchrotron facilities have been employed to study MRT due to the facility for easy generation of high flux and orthovoltage x rays (Hadsell et al. 2013). Although synchrotron MRT devices have been shown to be promising, several limitations prevented its applications.

The major limitation is the limited availability of such facilities for use in scientific research. Building a synchrotron is very costly. The construction usually costs tens or hundreds of millions of dollars. Additionally, each beamline (a large synchrotron typically comprises 20 to 50 of beamlines) costs another two or three million dollars on average. Therefore, synchrotron MRT is not a candidate for widely spread research studies.

1.1.3 Advantages of Compact Carbon Nanotube (CNT) MRT System

Because of the limitation of synchrotron sites, much effort has been devoted to developing a novel compact dosimetric platform for MRT by researchers at the

University of North Carolina (UNC) at Chapel Hill. They have recently developed the first generation compact MRT system based on carbon nanotube x-ray technology. This MRT irradiator employs triode carbon nanotubes instead of the conventional diode configuration. The gate electrode exerts a strong electric force to extract the electrons from the CNTs. CNT emitters are bound to the surface of the cathode substrate to increase the current density. The CNT field emission x-ray source irradiator comprises a linear cathode array and a novel collimator alignment system. The application of CNT field emission source has many advantages over the conventional sources such as higher dose rate delivery, more stable tube current performance and more accurate dose distribution.

1.2 PRESAGE/Micro-Optical-CT 3D Dosimetry System

Accurate and comprehensive understanding and verification of MRT dose distribution is crucial to achieve the success of MRT. Although some preliminary 2D dosimetric measurements have been performed by the research group at UNC Chapel Hill, comprehensive 3D characterization has yet to be achieved. Therefore, engaging PRESAGE/Micro-Optical-CT 3D Dosimetry system to measure the dose with a resolution on the micrometer scale should provide valuable measurements. By bringing in a completely independent outside dosimetry measurement, the MRT output can be verified.

Nevertheless, characterizing the dosimetry of MRT system output is extremely

challenging because of the very small fields involved. The first challenge is to find a combination of the dosimetry material and a reading device, which can allow an optimized response of the former. Here, we propose to introduce a novel in-house micro-optical-CT 3D dosimetry system utilizing a radiochromic plastic dosimeter (PRESAGE®), which has potential to characterize MRT deliveries with very high resolution in 3D.

1.2.1 PRESAGE®

Since 1984, because of the general tissue equivalent and high sensitivity features, many different gel and plastic materials have been developed for 3D radiation dosimetry. Some attractive features and advantages of PRESAGE dosimeter over gel dosimeter (both polymer gel and radiochromic gel) include its lack of sensitivity to the oxygen (polymer gel) or diffusion (radiochromic gel). Further, the PRESAGE dosimeter is solid, shapeable and requires no supporting container, therefore, it is easy to handle. (Alqathami et al. 2013) Previous investigations demonstrate linearity for the dose response in the dose range of 1Gy~30Gy. (Alqathami et al. 2013)

PRESAGE® was first introduced in 2006 as a compatible material with 3D dosimetry by optical CT. (Adamovics and Maryanski 2006) It consists of a polyurethane matrix, doped with a halogenated hydrocarbon free radical initiator and the leucodye leucomalachite green (LMG). (Oldham, M. 2014)

Free radicals generated from the radiolysis of the halogenated hydrocarbon

bond upon irradiation oxidize the LMG dye leading to a change in absorbance (indicated in figure 1). The change in absorbance is linear with respect to the absorbed radiation dose. (Juang et al. 2013)

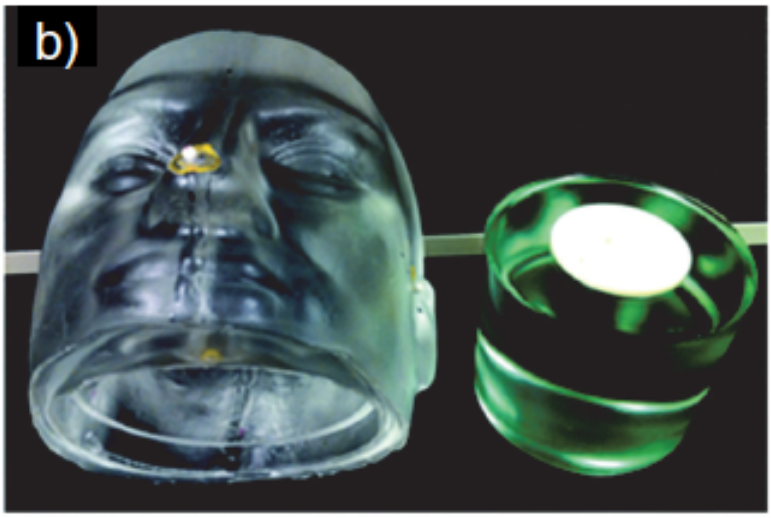

Figure 1 Color Change Due to Irradiation. Photograph of un-irradiated (left) and uniformly irradiated (right) dosimeters of the same formulation. (Oldham, M. 2014)

The absorbing nature of the PRESAGE material in Optical CT imaging turns out to be meaningful because the scattered light can be minimized and therefore narrow beam geometry is not necessary. This could save a great deal of effort in developing a collimating system and also largely increase the sensitivity of the Optical-CT imaging.

1.2.2 Micro-Optical CT 3D Scanner

The only compatible readout device for PRESAGE dosimeter is Optical CT so far. Optical Computed Tomography (Optical CT) was introduced to the research field in 1996. The technique is similar to x ray CT in many ways except using visible light as the

imaging radiation than X ray. Due to the relatively small size of the dosimeters, rotating of the dosimeter has been made more practical and convenient than rotating the source/detector. During the rotating, line integrals of attenuation are acquired at different views of the object and finally a Filtered-Back-Projection reconstruction can provide a 3D image set.

Because of the consideration of minimizing the stray light artifact, the parallel-beam geometry (shown in figure 2) is selected over the cone-beam geometry.

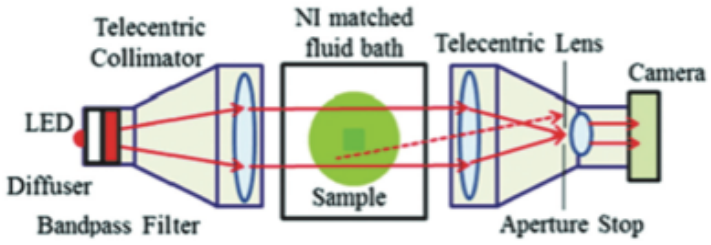

Figure 2 Parallel-beam Geometry. (Oldham, M. 2014)

Telecentric lens were used for both light source and camera, which further reduced the stray light contamination of the image, which greatly improve the image quality. (Oldham, M. 2014) However, isotropic and high-resolution 3D dosimetry is still not readily achievable even with these novel designs.

1.2.3 Characterization of microbeams irradiated by two MRT systems

In order to valid the accuracy and effectiveness of CNT MRT system, we designed two experiments: three strips irradiated by compact CNT MRT system and multi-beams irradiated by namely, Multi-beam MRT system (a commercialized x ray

irradiator collimated by a customized multi-beam collimator). My primary job is optimizing the DmicrOS system in order to improve the image quality and to achieve the ultra-high-resolution (fifty microns) of the images, from which accurate dosimetric information (such as Percentage Depth Dose (PDD), Peak-to-Valley Dose Ratio (PVDR) and beam width (FWHM)) can be obtained. Two types of experiments irradiated by different MRT systems will be compared and evaluated based on these dosimetric data. Finally, both results will be compared with the 2D dosimetric data collected by UNC at Chapel Hill.

2. Materials & Methods

In this section, the basic design and standard operating systems of both Multi-beam MRT (a commercialized x ray irradiator + a customized multi-beam collimator) and CNT MRT systems will be firstly presented. Secondly, the dosimeter material, basic design of DmicrOS system as well as the standard operating procedures will be introduced. Lastly, the methods of optimizing system, stray light correction, 2D and 3D data analyzing will be provided.

2.1 Multi-beam MRT System

The multi-beam MRT is owned by University of North Carolina Linberger Clinical Cancer Center, which was originally designed for small animal irradiation studies. This system was employed in this study for a comparison study of the performance with that of CNT-MRT.

2.1.1 Basic Components and Design

2.1.1.1 Source

The MRT irradiator comprises a commercialized x ray source: RadSource RS2000 (160kV, 25 mAs).

2.1.1.1 Multi-slit collimator

The multi-slit collimator (shown in figure 3) is made of 18 cerrobend strips being placed in grooves on a cerrobend plate. The collimator is mounted under a large single focal spot. The collimator collimates the source into multiple thin strips.

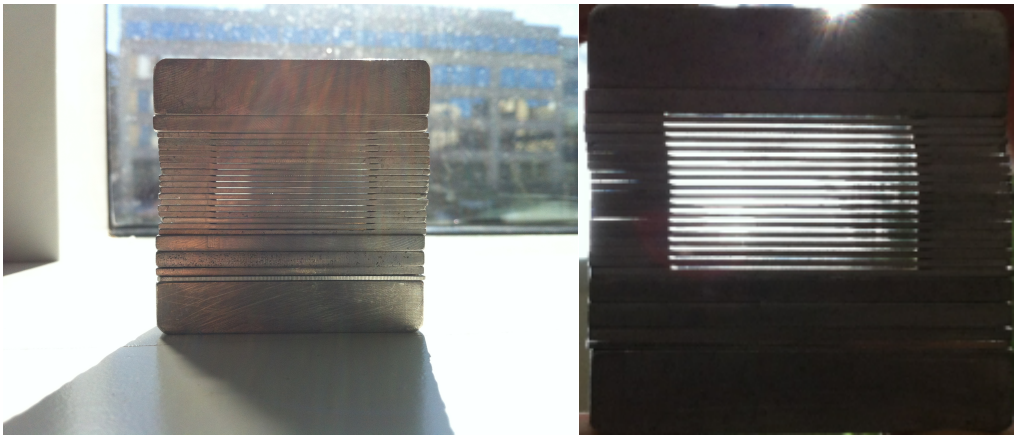

Figure 3 Multi-slit Collimator. The figure on the right is a zoom in collimator image of the one on the left. Light fields can be easily seen on the right image.

2.1.2 Typical Delivery Procedure

Some illustrations of the typical operating procedures are shown in the figure 4. The summarized steps are: 1. Place the frame based on laser localization; 2. Mount the collimator on the frame (the sample is placed under the frame); 3. Attach the sample (dosimeter/film) on a scale and send it to the isocenter of the beam aligned by the laser (under the frame); 4. Calculate the time needed for delivering a certain dose. As can be seen, all of these alignments must be done manually.

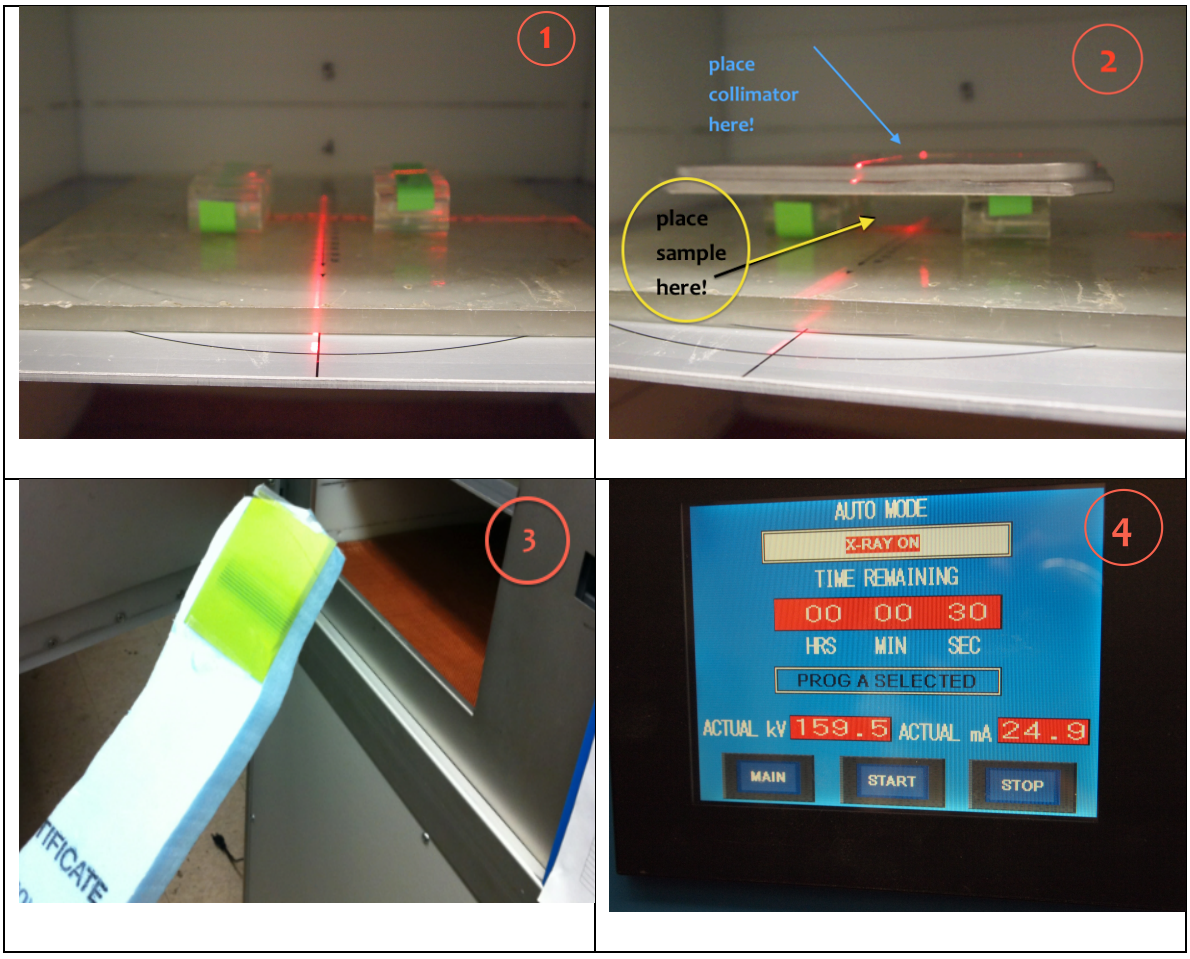

Figure 4 Operating Procedures of Multi-beam MRT System.

2.2 Carbon Nano-Tube (CNT) MRT System

This MRT system owned by the Physics Department and the Radiation Oncology Department of University of North Carolina at Chapel Hill. This was the first generation compact MRT irradiator employed Carbon-Nano-Tube cathode techniques and novel collimating alignment system. This was originally designed for small animal irradiation studies.

2.2.1 Basic Components and Design

This CNT-MRT (shown in figure 5) employs triode carbon nanotubes instead of the conventional diode configuration, in which a gate electrode is added in between the cathode and the anode. This will allow the X ray production to only depend on the voltage between the gate and the cathode and be independent of the anode voltage. The gate electrode exerts a strong electric force to extract the electrons from the CNTs. This is called field emission. This type of emission uses a different mechanism than thermionic emission, which is commonly employed by a regular x ray tube. Additionally, CNT emitters are bounded to surface of the cathode substrate and to assist with the electron extraction.

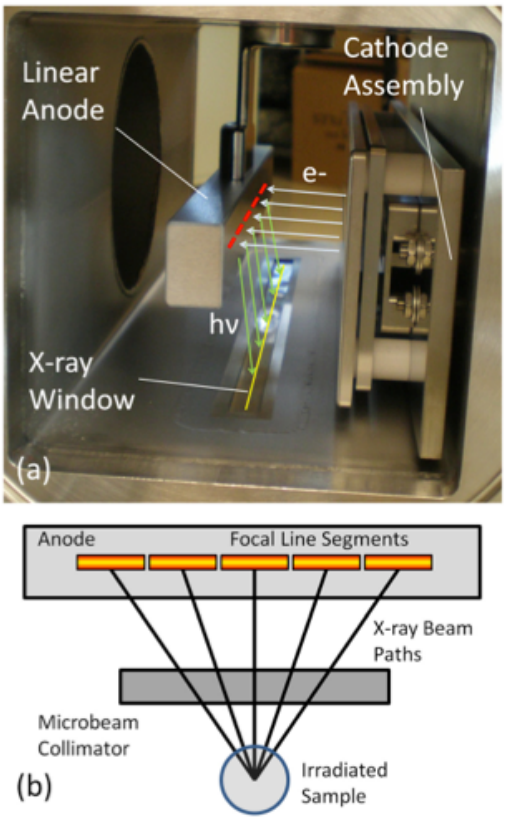

Figure 5 The Basic Components of Novel Compact Carbon Nano-Tube (CNT) MRT device (inside view). (Hadsell et al. 2013) (a) indicates the electron beam (white) shooting out of the cathode assembly, depositing on the focal line segments (red) in the anode and then finally the formed X ray beams (green) are projected onto the window (yellow). (b) illustrates the X ray beams paths are originated from the segmented focal lines, passes through the microbeam collimator and finally deposit onto the irradiated sample.

Besides these modifications on the source, the irradiator is considered unique because of two innovative designs: the linear cathode array and the collimator alignment system.

2.2.1.1 Linear cathode array

Figure 6 demonstrates the design of the linear cathode array.

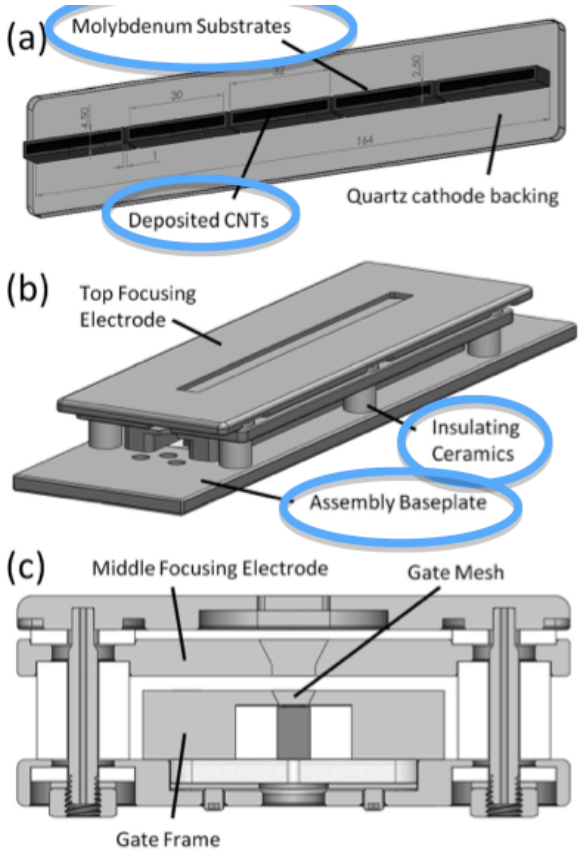

Figure 6 Linear Cathode Array. (Hadsell et al. 2013) (a) shows the linear cathode array consists five substrates with CNTs deposited on each of their surface. (b) and (c) show the dual electrodes and a gate mesh.

The focal spot is segmented into five substrates instead of using a single large focal spot as most of the cases in commercialized X ray source (shown in figure 7).

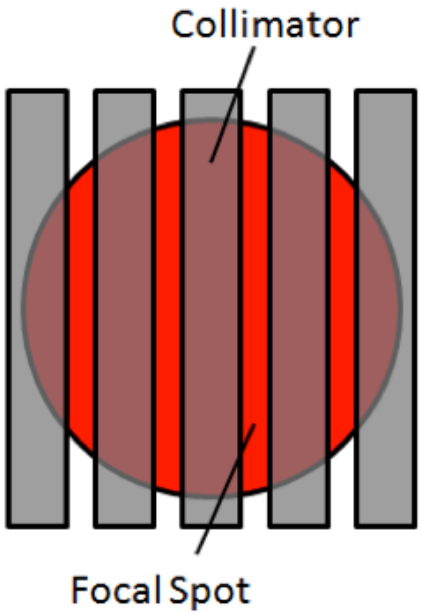

Figure 7 Single Large Focal Spot Being Collimated by Thick and Long Collimator.

Because of most current flux being saved by segmenting the large focal spot in CNT x-ray irradiator, the design in return largely increases the dose rate delivery without causing as much anode heat as regular x ray source. As a result, 75 mA tube current for each focal line is achieved in a short pulse of 0.1s. (Hadsell et al. 2013)

2.2.1.2 Collimator alignment system

In order to shape the cone beam into a sub-millimeter fan beam, the collimator was fashioned from two stainless steel gauge blocks clamped together against two glass spacers. Additionally, the collimator alignment system was designed to be able to translate perpendicularly to the plane of gantry rotation, pitch in a direction above the gantry plane and roll around the axis of the cone beam. In this way, the alignment

system can successfully select out the appropriate planar portion of the cone beam that would coincide with the gantry's plane of rotation so as to ensure the multiple beams would overlap. By doing this, a final microbeam with dimensions of 5mm x220um can be produced. (Hadsell, M. 2013)

Figure 8 demonstrates the design of the novel collimator alignment system.

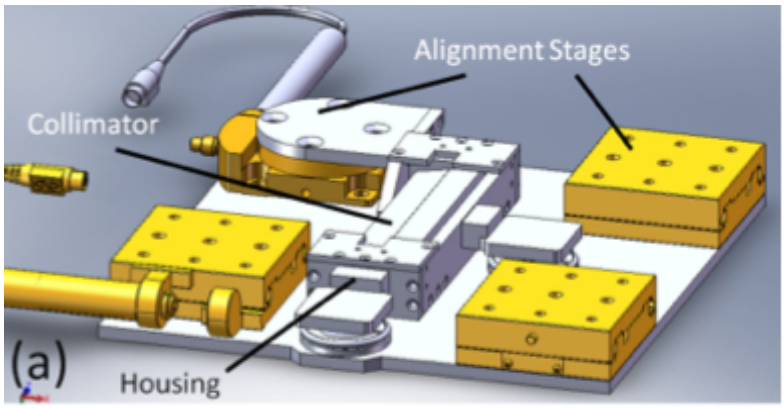

Figure 8 Collimator Alignment System.(Hadsell et al. 2013)

2.2.2 Typical Delivery Procedure

Figure 9 (1) shows the irradiated sample was first immobilized manually on a train. Then, as indicated by figure 9 (2), the train was placed at the tip of the track (with the assistant of laser beams) so that the train was precisely moved along the track toward the cathode. This process was precisely operated by the computer system, in order to place the sample to the exact same position every time. There is a console outside of the radiation room from where dose calculation (dose rate x times) can be performed and then the radiation can be delivered.

Note that to avoid the excessive exposure, the whole procedure is required to perform in the dark.

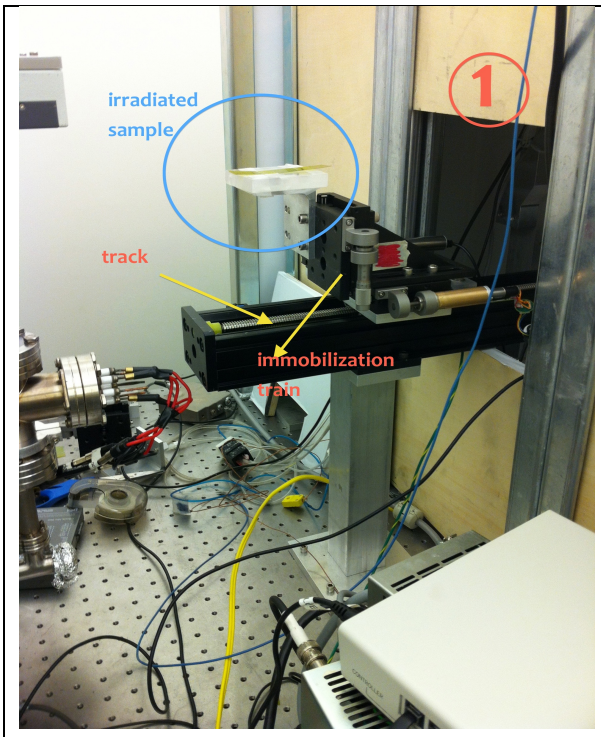

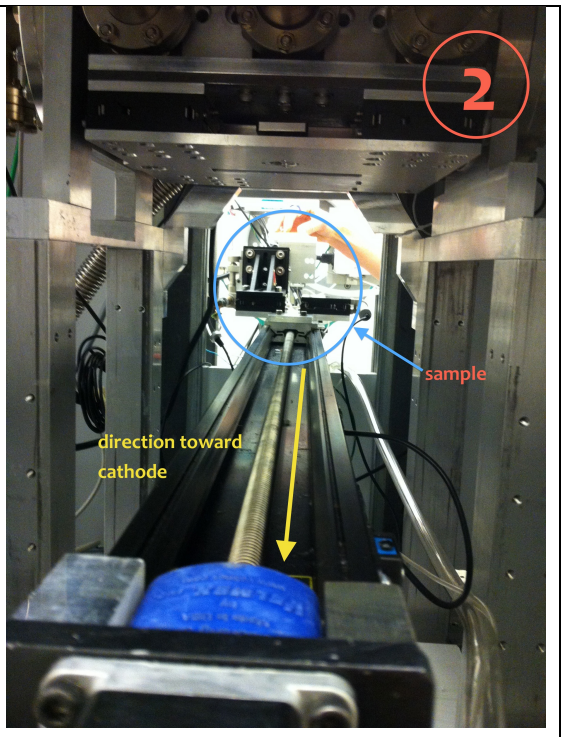

Figure 9 Immobilization and Alignment. The sample was first fixed on the immobilization train and then sent to the irradiation position.

2.3 PRESAGE®/Micro-Optical CT 3D Dosimetry System

2.3.1 PRESAGE®/Micro-Optical CT 3D Scanner

For convenience, we label our PRESAGE Dosimeters to be UNC_A, UNC_C, UNC_D, UNC_E, UNC_F. The information of thesis dosimeters' dimensions and formulations can be found in table 1.

Table 1 Dimension of Dosimeters.

	Formulation	Height (mm)	Diameter (mm)
UNC_A	Meo-DEA	21.98	25.37
UNC_C	Meo-DEA	21.92	25.08
UNC_D	Meo-DEA	21.85	25.11
UNC_E	Meo-DEA	27.00	24.55
UNC_F	Meo-DEA	27.02	24.64

2.3.1.1 Basic component and design

Duke Micro Optical-CT Scanner (DMicrOS) (shown in figure 10B) was designed, constructed and optimized to characterize this MRT study. It includes a light source (BI telecentric lens, TC-series), an aquarium, a rotating stage, imaging lens and a CCD camera (Basler PiA 160035gm). The dosimeter is screwed on the middle of the stage. A matching fluid filled in the aquarium. By acquiring projection images at discrete angles as the stage rotating around, a 3D optical imaging matrix can be reconstructed. Note that

the distance between CCD camera lens's surface to light source lens surface is 29cm(shown in figure 10A). The glass water tank (6.5mm x 6.8mm x 7.0mm) (shown in figure 10A) is placed in between the CCD camera and the light source.

Table 2 summarized the basic information of the camera employed in the DMicrOS respectively.

Table 2 Basic Information of the Camera.

Vendor	Basler
Model	PiA 160035gm
Sensor Type	CCD
Pixel Width	7.40 μm
Pixel Height	7.40 μm
Magnification	0.25

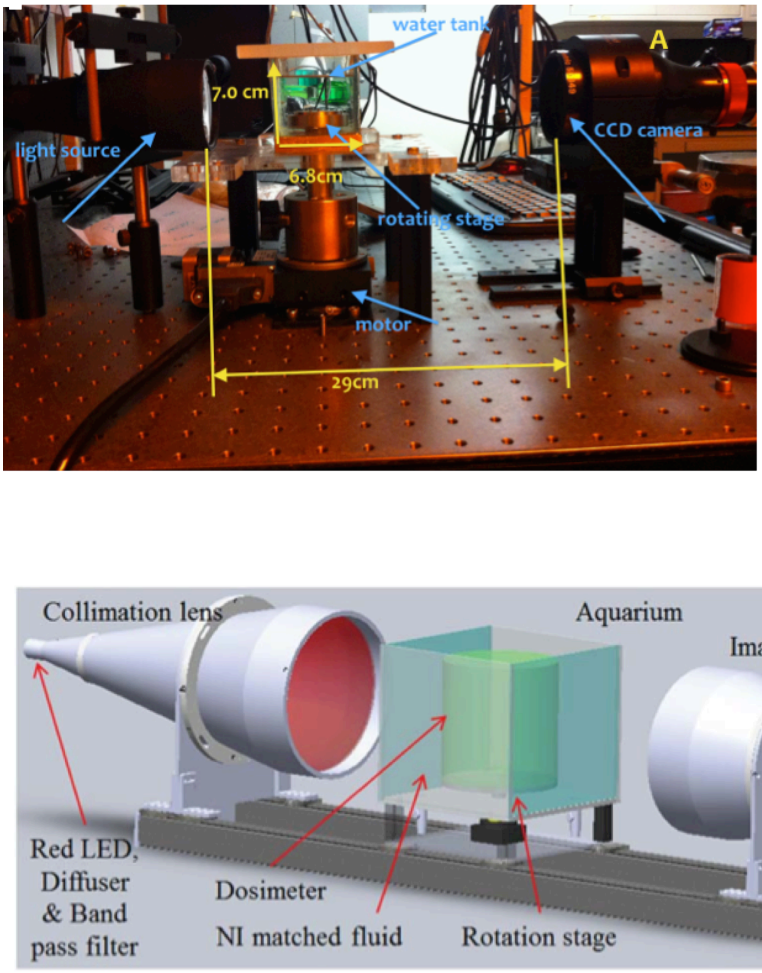

Figure 10 Basic Components of DmicrOS system. A: Photograph of the DMicrOS system in the lab shows the dimension information. B: Schematic of the prototype and light paths through the DMicrOS system (Thomas, et al. 2011).

2.3.1.2 Basic Testing of the Performance of Camera

Several important parameters that should be measured to characterize the basic performance of an imaging system are Signal-to-Noise Ratio (SNR), dynamic range, resolution in object space, largest FOV and MTF.

Dark images taken from five dosimeters' pre and post scans were analyzed to predict the noise level for the system, mean, standard deviation and the percentage of the full signal were provided in the result section.

Dynamic range of a sensor is defined by the largest possible signal divided by the smallest possible signal it can generate. The maximum practical dynamic range for this system is ~3800 (minimum signal to maximum signal is 100~3900 counts). For this particular system, the dynamic range was predicted by analyzing the maximum signal from the flood images and minimal signal from dark image of five dosimeters' pre and post scans, mean and standard deviation were provided in the result section.

The largest object's Field-Of-View (FOV) is 1608 pixels (HFOV) x1208 pixels (VFOV) (47.6 mm x35.8 mm). The images may be cropped to fit the actual dimension of the dosimeters. In this way, the image sizes can be largely reduced. The result section shows the actual FOV chosen by the five dosimeters.

MTF was obtained from Fourier transform of PSF. PSF was obtained by section 2.3.1.5.

2.3.1.3 Image acquisition

Prior to irradiation:

1) Robust Mounting of the dosimeters

Figure 11A shows medal barbs on the top of the rotating stage. As indicated in the figure 11B, two holes were drilled at the bottom of the dosimeter and screwed on the

rotating stage to match up with the medal barbs. A weight was placed on top of the dosimeter to avoid floating. This mounting of the dosimeter is essential since the exact position is required for pre and post scans. Otherwise, the post image will not be corrected correctly.

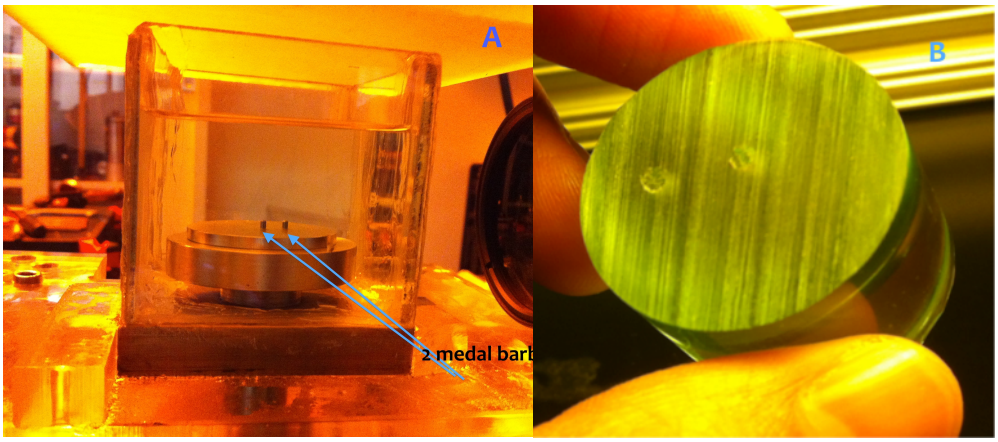

Figure 11 Robust mounting of the PRESAGE dosimeter in DMicrOS is critically important for accurate high-resolution dosimetry. A is a closer look at the rotating stage. The two medal barbs on the stage are to match up with the holes drilled at the bottom of the dosimeter as indicated as B.

2) Alignment of optical system

The physical alignment of the optical system is crucial to the image quality and therefore accuracy of the dosimetry analysis. Intensity gradient across field of view, suggests poor alignment. The alignment can be done manually.

3) Fluid matching

The goal of fluid matching is to find the fluid with the closest Refractive of Index (RI) to match up with that of the dosimeter. Octhl Methoxy Cinnamate (RI=1.542~1.561)

and Mineral Oil (retail) (RI=1.473~1.480) were mixed with arbitrary ratios initially. Screen shots were taken during this process (shown in figure 12) that different matching images could be compared to find the optimal ratio. A spectrometer was used to read out the refractive of index of the matching fluid. The group images shown in figure 13 indicate how the process can be done to find the optimal matched point.

Starting from a low Refractive-of-Index (RI), a single dark band is shown on both left and right outer edges of the dosimeter (a). As the RI increases, the dark band is reduced (b) more and more (c). At one point, the dark band is minimized and if keep increase the RI, dark band starts to show on the inside edges of the dosimeter (d). Keep increasing the RI, the dark band is pronounced (e) more and more (f). This suggests that the optimal point is at c.

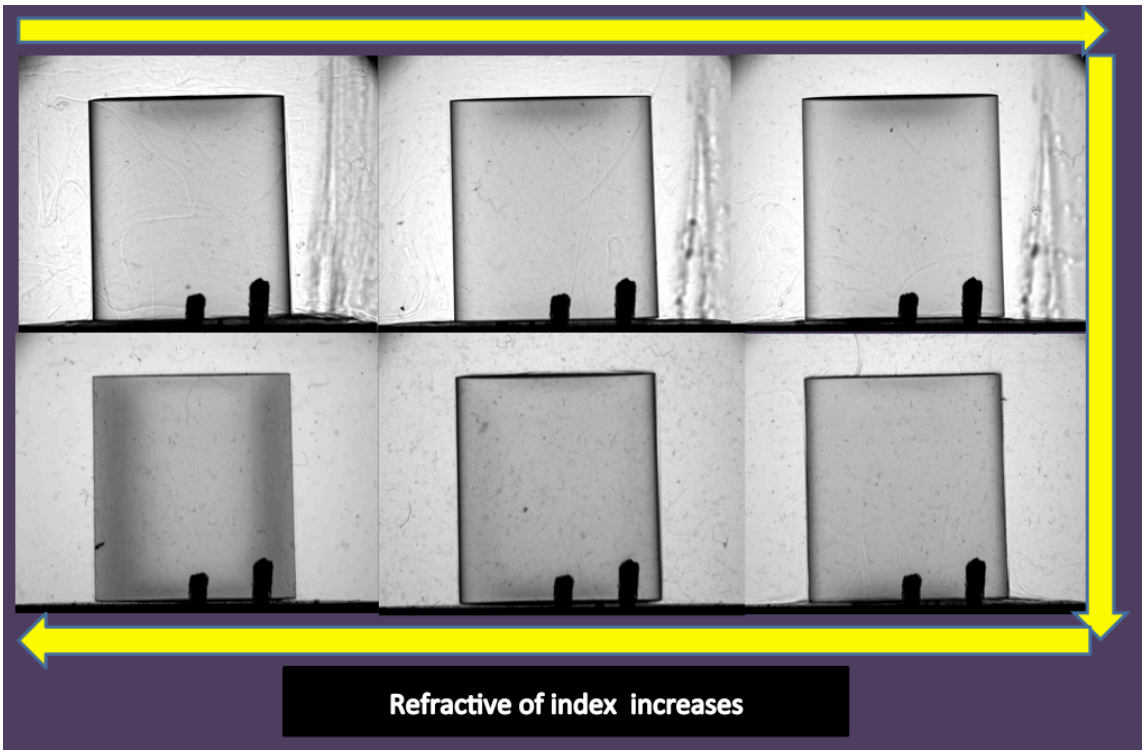

Figure 12 Fluid Matching Process for Dosimeter UNC_E. From a to f, show how the dosimeter looks in the fluid matching process. Optimal fluid match is show in figure c.

4) Acquisition settings

Exposure time (absolute value) is one of the most important acquisition parameters. The absolute value can be chosen based on this following principle: gives the maximum counts (permit maximum light passing through) that will not saturate the image (The saturation counts number is 4950).

The projections of the dosimeter were acquired as 32 bit real (floating) big endian images. The camera needs to be set to Mono 16.

During the scanning, a pre-dark image, a pre-flood image and 720 pre-scan images will be acquired. The actual acquisition time for acquiring a complete image set is about~ 1 hour.

5) Chose FOV

As stated above, the FOV was cropped to adequately cover the whole dosimeter area. A "360 degrees test" was performed before the real acquisition of the projected images. This test can ensure that the whole rotation is within the field of view. The width and height parameters will be needed for writing the ScanInfo file.

6) Initialize motor

This allows the motor going back to the original position every time before scanning recorded. Initializing motor is required whenever before scan starts.

Post the Irradiation:

1) Post images scanning time: The dosimeter should be scanning as soon as the irradiation has been done to minimize the dose variation as time.

Note that during the whole scanning time, the dark environment will be required (no room light) all the time to avoid unnecessary exposure from infrared light and sunlight.

2) Storage of the dosimeter: The best way to preserve the dose information after the irradiation is storing the PRESAGE dosimeter in the refrigerator (Gorjiara et al. 2013).

2.3.1.4 3D Image Reconstruction and Dosimetry Analysis with MATLAB

Before reconstruction, a ScanInfo file must be created/modified in order to perform the correct reconstruction for each individual dosimeter. All the images (pre-dark, pre-flood, pre-image, post-dark, post-flood, post-image) were imported to a customized MATLAB Reconstruction GUI (shown in figure 13) in the lab in order to be

reconstructed to 3D.

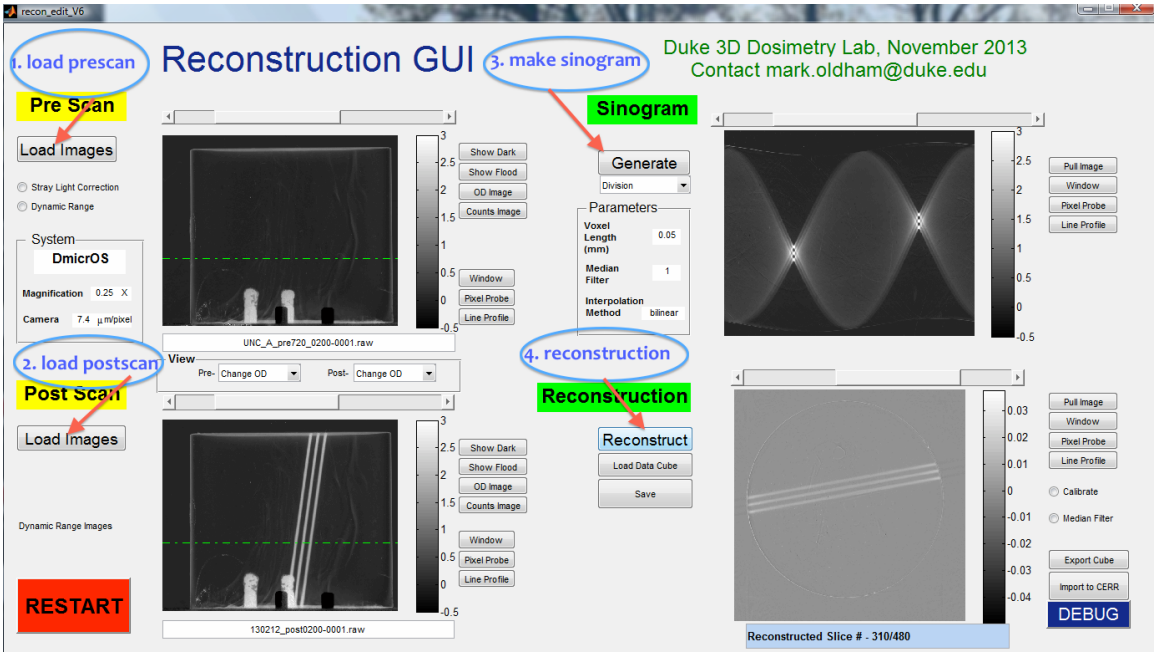

Figure 13 Reconstruction GUI Interface. Procedures are indicated: 1. Load prescan. 2. Load post scan. 3. Generate Sinogram. 4. Reconstruct.

During the reconstruction, the dark images (pre-dark and post-dark) need to be subtracted from the projection images (pre-scan images and post-scan images) respectively. Then, the flood images (both pre-flood and post-flood) need to be divided from the projection images (pre-scan images and post-scan images) respectively.

A ramp filter will be needed for the Filtered-Back-Projection reconstruction. Other parameters for the reconstruction include reconstruction resolution, desired reconstruction length and Center–Of-Rotation (COR). The resolution for this study is $50um$. The reconstruction length was chosen slightly larger than the diameters of the

dosimeter (In this study is 30mm). The COR can be estimated from the post images. Screen shot should be taken during this process to find the optimal COR.

2.3.1.5 Residual Stray light correction

Like X ray CTs, optical CTs are also susceptible to numerous artifacts such as rings, beam hardening, attenuation, motion and etc. (Oldham, M. 2014) The stray light artifact can be a even more serious problem for such a small geometry(the spacing in between beams can be easily contaminated by stray light).

The stray light artifact is a result completely caused by scatter and aberration. The stray light effect has been illustrated in figure 14:

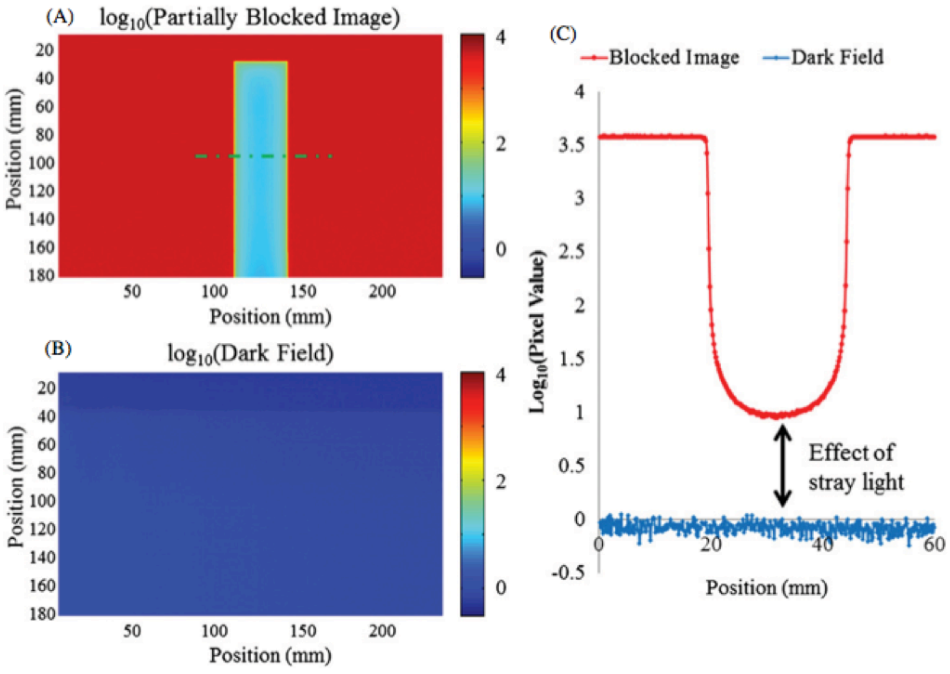

Figure 14 The Stray Light Effects. Behind the block image, the dark field count values are expected. However, the signal is higher than the background noise. Effect of stray light can be illustrated as the difference between the signal and background noise. (Thomas et al. 2011)

The Point Spread Function (PSF) of the system is defined as an image of a point source. An output image of an object can be regarded as a two dimensional convolution of an "ideal" image with the PSF. The blurriness of the PSF causes the blurriness of the image. The effect of stray light is to cause additional, undesired blurring in the PSF. A Stray Light Correction is to deblur (deconvolve) the PSF from the output image. This was performed before the reconstruction of each data set. Several of functions in MATLAB can readily deconvolve the image such as "deconvlucy()". Therefore, the remaining job is to determine an accurate PSF.

1) PSF measurement:

Physical aperture experiments were performed with different sized apertures (50 μm , 200 μm , 1630 μm and 5000 μm). The FOV was opened to the maximum size and the maximized absolute exposure time was used. Then, all the raw images were imported to the ImageJ. The radial profiles were taken for each aperture image, which can average the line profiles taken in all the directions. Then, all the results were then imported to the Excel worksheet (version 2011) for analysis.

2) PSF generation:

Take out of the noise floor of each line profile. Normalize the intensities for each line profile, so that area under each curve stays unity. It is known that the smallest aperture is the closest to the ideal situation. However, the profile drops quickly and will not give much information as the noise floor was reached. However, the larger apertures allow

more lights into the system and illuminate regions of pixels at greater distances from the aperture. So, the smaller aperture best predict the behavior of the PSF around the center pixel and the larger ones best predict the behavior of PSF away from the center. (Thomas et al. 2011) In the Excel, the normalized four gaussian shape radial profiles will be superimposed into one figure. This is named 1D PSF.

3) PSF implement:

The 1D PSF was resampled：the same value was assigned to all directions on the same concentric circle to form a 2D PSF, namely. This 2D PSF is a radial symmetric matrix. A build-in MATLAB function "deconvlucy()" was used to deconvolve the images with PSF.

4) Validation tests:

An opaque block was placed in between the camera and the aquarium. Behind the block an extremely low count values (~0) was expected. However, instead, the signal can be seen is significant higher. This difference in between is caused by scattered light, both aberrations and diffractions. The PSF is applied to this whole block image to deconvolve the original image.

Choose the most attenuated slice from the reconstructed image data set. Take line profiles across the strips with and without the removal of the stray light. Superimpose these two line profiles with the dark noise floor and then a comparison analysis can evaluate the effectiveness of the correction.

2.2.3 Irradiation Experiment

2.2.3.1 Conventional X-ray tube Irradiator MRT multiple beam experiment

A regular x-ray source combined with the multi-slit collimator was used to deliver the multiple microbeams.

2.2.3.2 CNT-MRT three strip beam experiment

Three angled beams were delivered by CNT-MRT as indicated in figure 15:

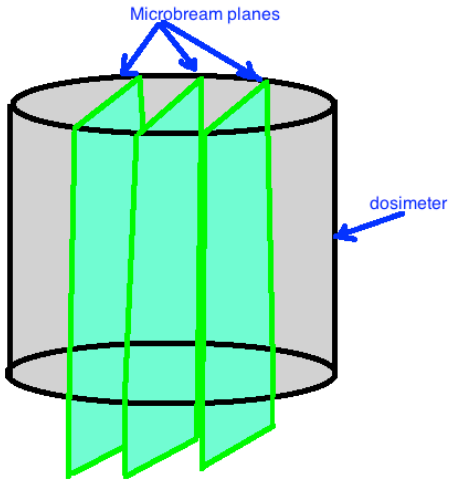

Figure 15 Three Strips Impingent on Dosimeter. Three microbeam planes cut through the dosimeter from the top to the bottom.

2.2.3.3 2D dosimetry Film verification

The film calibration curve was created using the 6MV X-ray beam from a clinical radiation treatment machine (VARIAN 600CD) source installed in the Radiation Oncology Department of the Duke University Hospital. Then, some experimental films were irradiated by both irradiators at UNC Chapel Hill Physics department (regular x ray irradiator and three x ray irradiator) with the UNC_E and UNC_F dosimeter

respectively. All the films were scanned by a lab scanner: EPSON EXPRESSION 1000XL at a resolution of 200 dots per inch. The resulting images were saved as TIF file. The three color-channels were split and only the red channel data were analyzed owing to its cleaner response than the other two colors (Annabell et al. 2012). The resulting images were analyzed with ImageJ/MATLAB. The PVDR, PDD and FWHM data can be acquired by similar methods as analyzing the dosimeters. The detailed calibration and scanning procedures can be found in Appendix A and B.

3. Results

3.1 Basic Testing

3.1.1 Modulation-Transfer-Function (MTF)

The MTF shown as figure 16 was obtained by fourier transform the Point-Spread-Function(PSF).

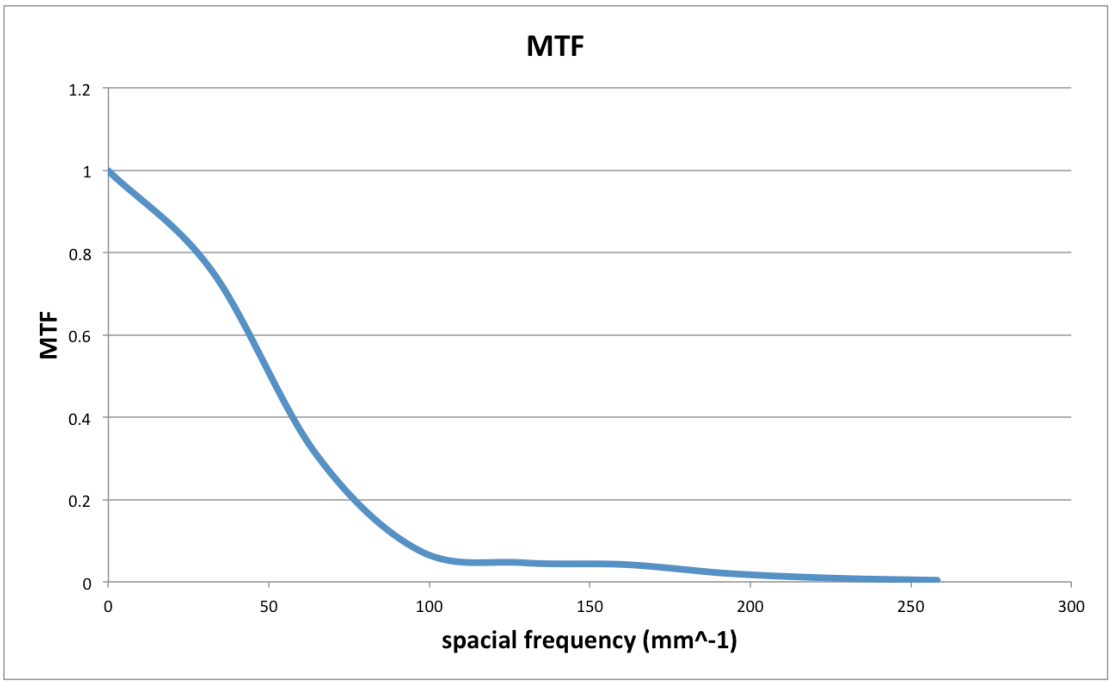

Figure 16 MTF of DmicrOS

3.1.2 Signal-to-Noise Ratio (SNR)

The dark noise value was taken from average measurement in ImageJ for each of the ten dark images. The mean and standard deviation were calculated as table 3. The maximum signal was estimated from averaging the ten flood images. The mean and standard deviation were calculated as table 4.

Table 3 Dark Noise Levels of DmicrOS.

Mean (counts)	std (counts)
3.8	0.04

Table 4 Flood Signal levels of DmicrOS

Mean (counts)	std (counts)
3952.9	84.8

Because SNR was defined as the ratio of the mean pixel value to the standard deviation of the pixel values, SNR for flood count image is 46.6.

3.1.3 Pixel Size in Object Space

The pixel size is 29.6 μm which is pixel width (or pixel height) (from table 2) divided by magnification (from table 2). (7.4 μm /0.25). This suggests that any object in physical space smaller than 29.6 μm would not be able to be detected. The resolution for this case is chosen to be 50 μm, which is close to the camera's maximizing detectability.

3.1.4 Dynamic Range of Sensor

This camera has a dynamic range (3800 counts), which enables to capture shadow detail and highlight detail at the same time. The dynamic ranges largely vary with the performance of the optical alignment.

3.1.5 Scanning/Reconstruction/Correction time scale

The time to acquire 720 projections is about 1 hour if the "average-images" is chosen to be five times. The time to reconstruct 720 projections is 15min. The time to correct 720 projections is less than 1 min.

3.1.6 FOV

The largest FOV is 1608 x1208 pixels. It can be cropped in smaller FOV depending on the dimension of the dosimeters. Table 5 shows the FOV choosing for each dosimeter.

Table 5 FOV Chosen.

Dosimeter	FOV (Height x Width)
UNC_A	810 x 1000
UNC_C	810 x1050
UNC_D	810 x1050
UNC_E	923 x1281
UNC_F	923 x1281

3.2 Stray Light Correction

3.2.1 PSF measurement (Aperture Images)

The PSF is applied to this whole block image to deconvolve the image. Results below show difference between signal and background noise is cut down to almost one half.

3.2.2 PSF generation (1D Merged PSF & 2D PSF)

1D PSF (figure 17 left) shows the intensity drop (in one direction) from the center of the point source. 2D PSF (figure 17 right) shows the intensity drop (in two dimensions) from the center of the point source.

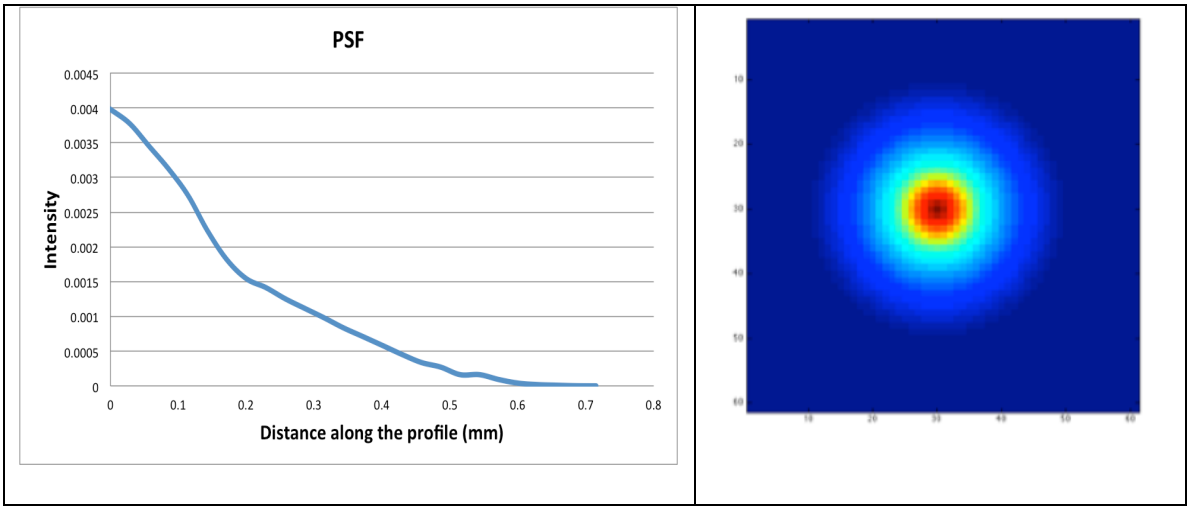

Figure 17 1D Merged PSF (left) and 2D PSF (right).

3.2.3 PSF Verification Tests

3.2.3.1 Block tests

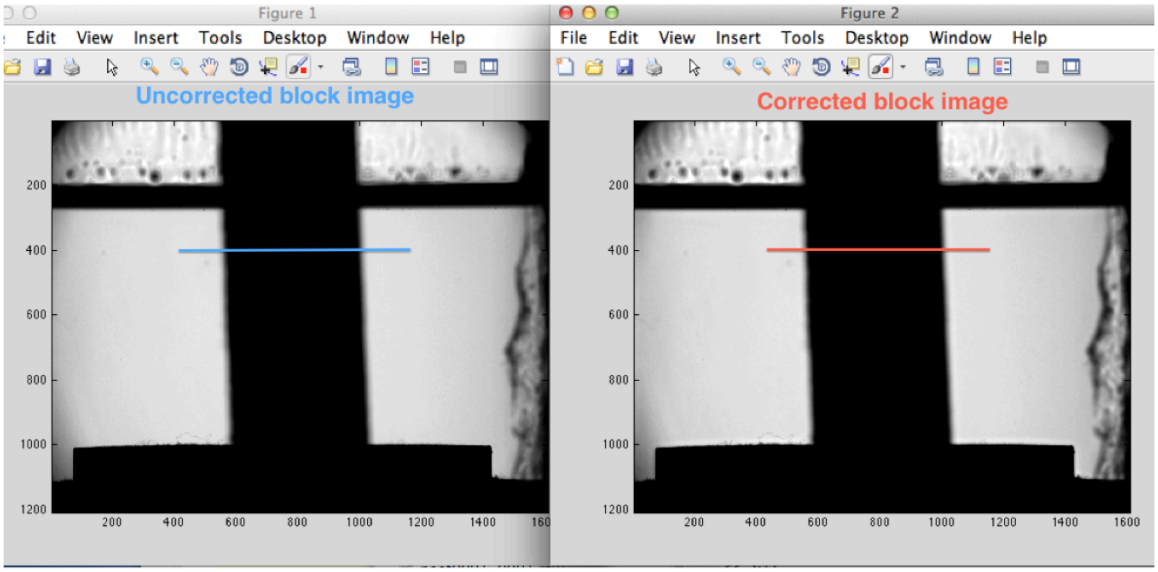
Figure 1
Edit View Insert Tools Desktop Window Help
Uncorrected block image
Figure 2
File Edit View Insert Tools Desktop Window Help
Corrected block image

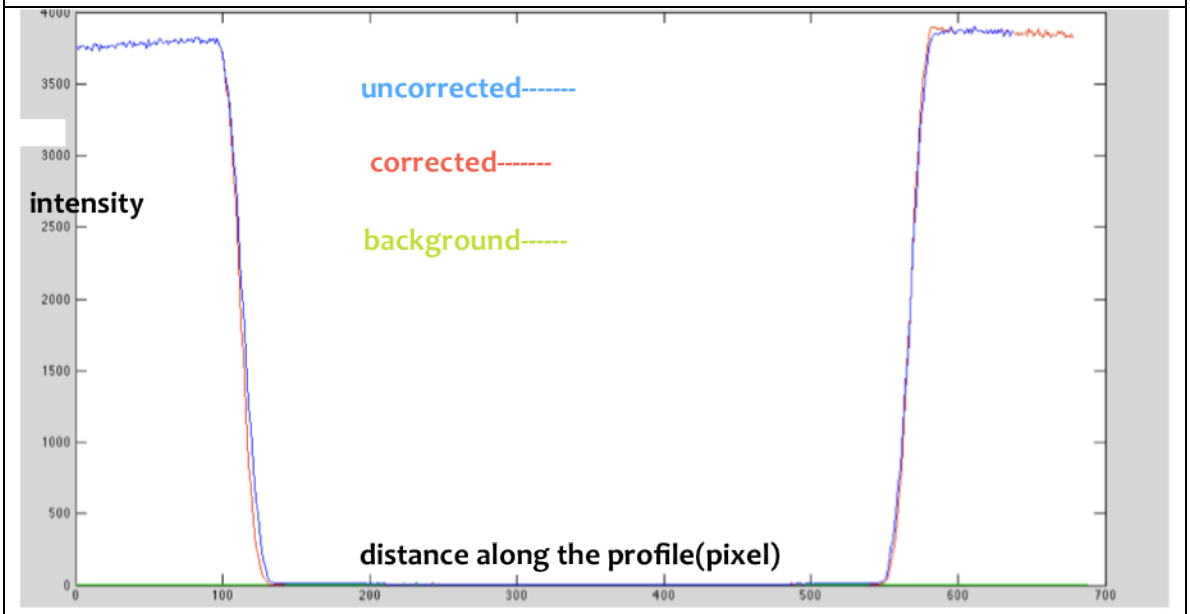
uncorrected-------
corrected-------
background------
intensity
distance along the profile(pixel)

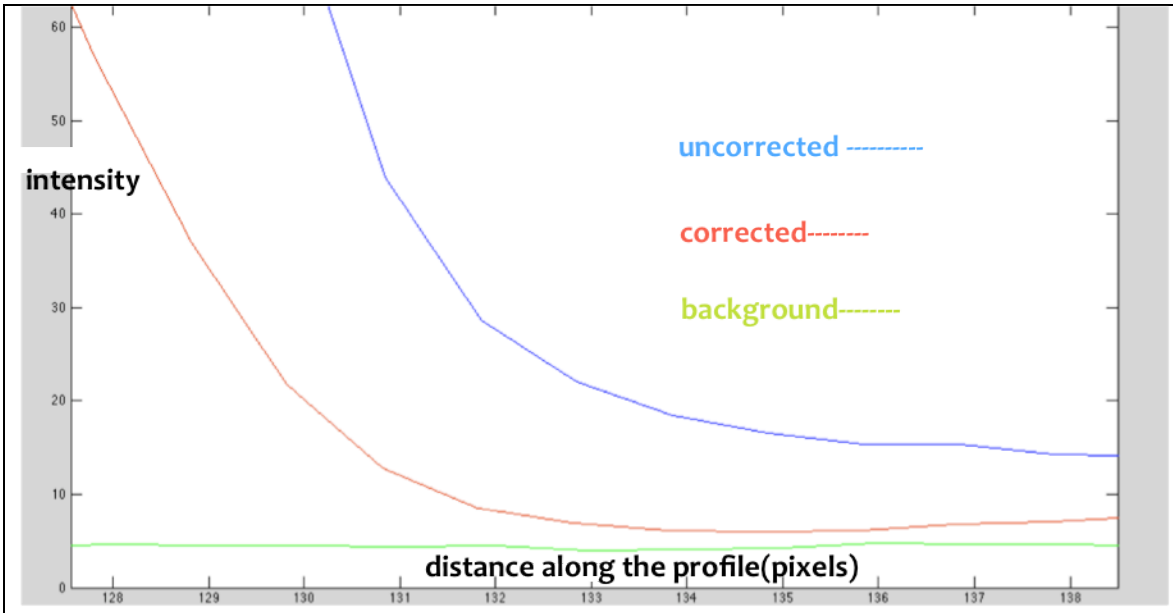

Figure 18 Stray Light Verification Test on Block Images. The top row shows an uncorrected block image (left) and a corrected block image (right). A line profile was taken for each and superimposed into the middle row. As its left corner being zoomed in at the bottom row, the red curve brings about more than 50% counts down to the noise floor (dark).

3.2.3.1 Single slice tests

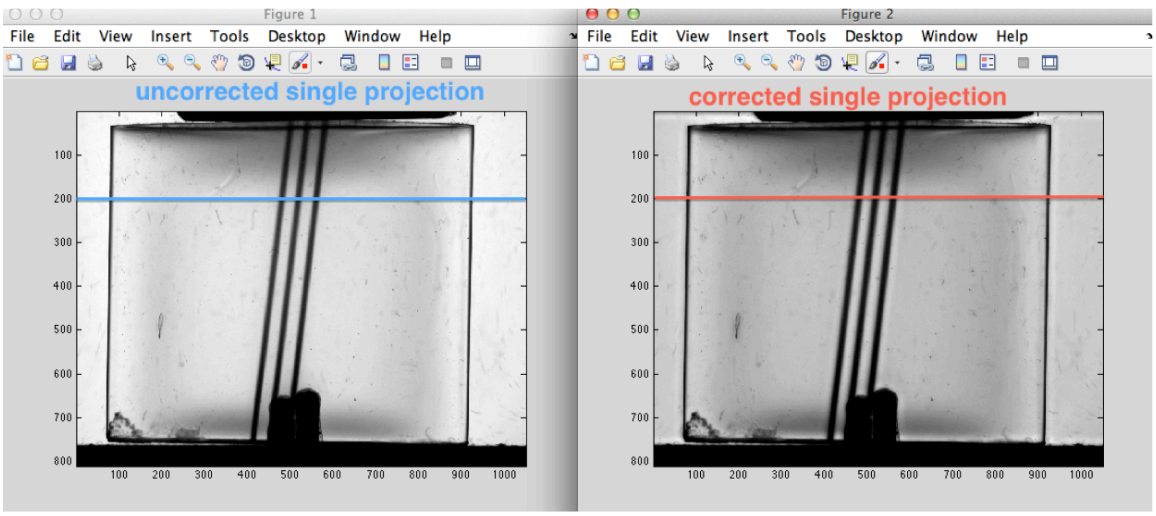

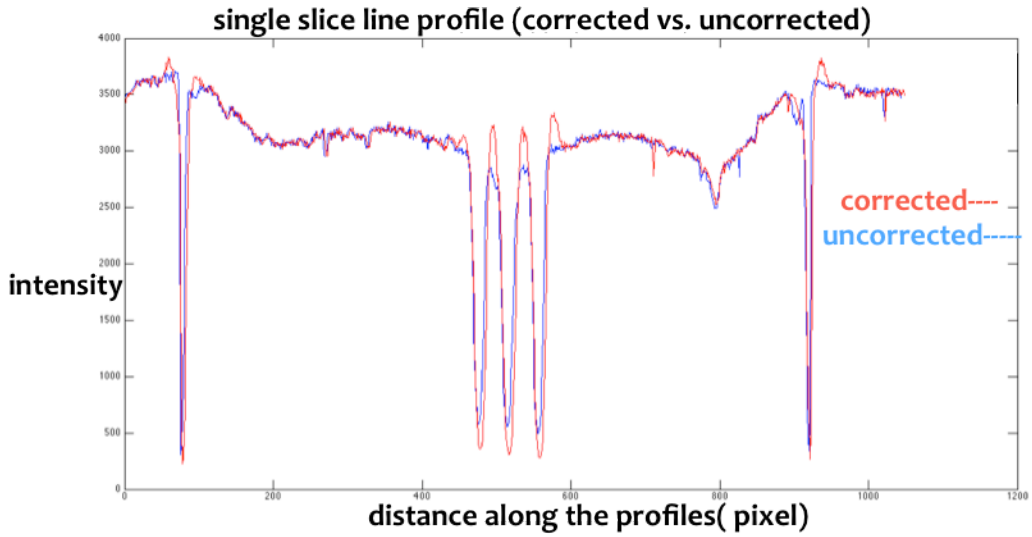

Figure 19 Stray Light Verification Test on Single Most Attenuated Projection. The top row shows an uncorrected image (left) and a corrected image (right). A line profile was taken for each and superimposed into the bottom image. As can be seen, the red curve brings about 320 counts down at the valley while adding some unexpected signal to the peak.

3.2.4 PSF Correction Result

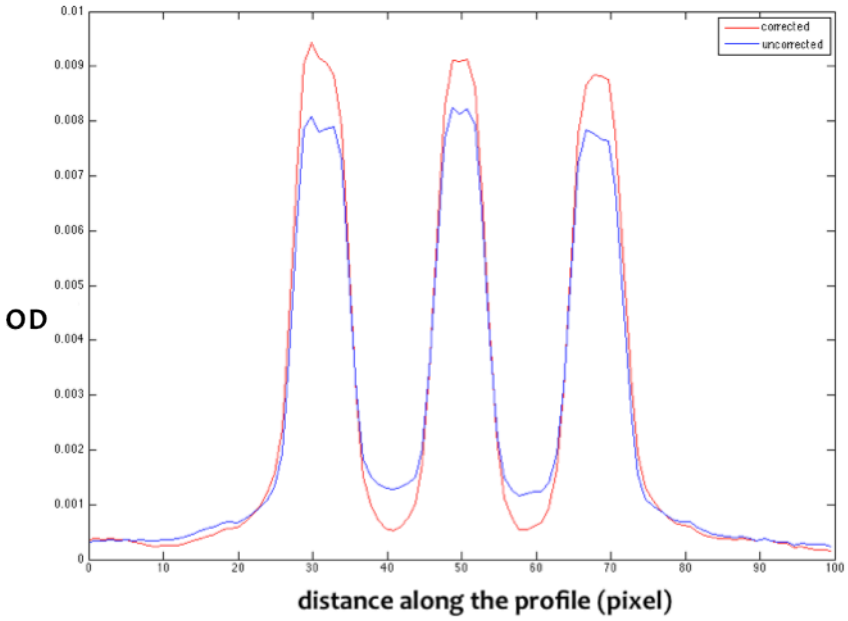

Figure 20 Corrected and Uncorrected Images from 3 strips MRT study. The corrected beam profiles were taken from the center slide of the reconstructed cube of UNC_A. (correction was applied to all the projections, both pre and post, before the reconstruction)

3.3 Multi-beam MRT Irradiation Experiment

From the reconstruction GUI, several post irradiation images (with the most attenuated beam direction) (shown in figure 21) were pulled out as well as their OD images. As can be seen in figure 21, there were thirteen strips delivered but with clearly beam divergence. Preliminary analysis of microbeam characteristics was performed on a ROI averaged across the central 5mm of the dosimeter.

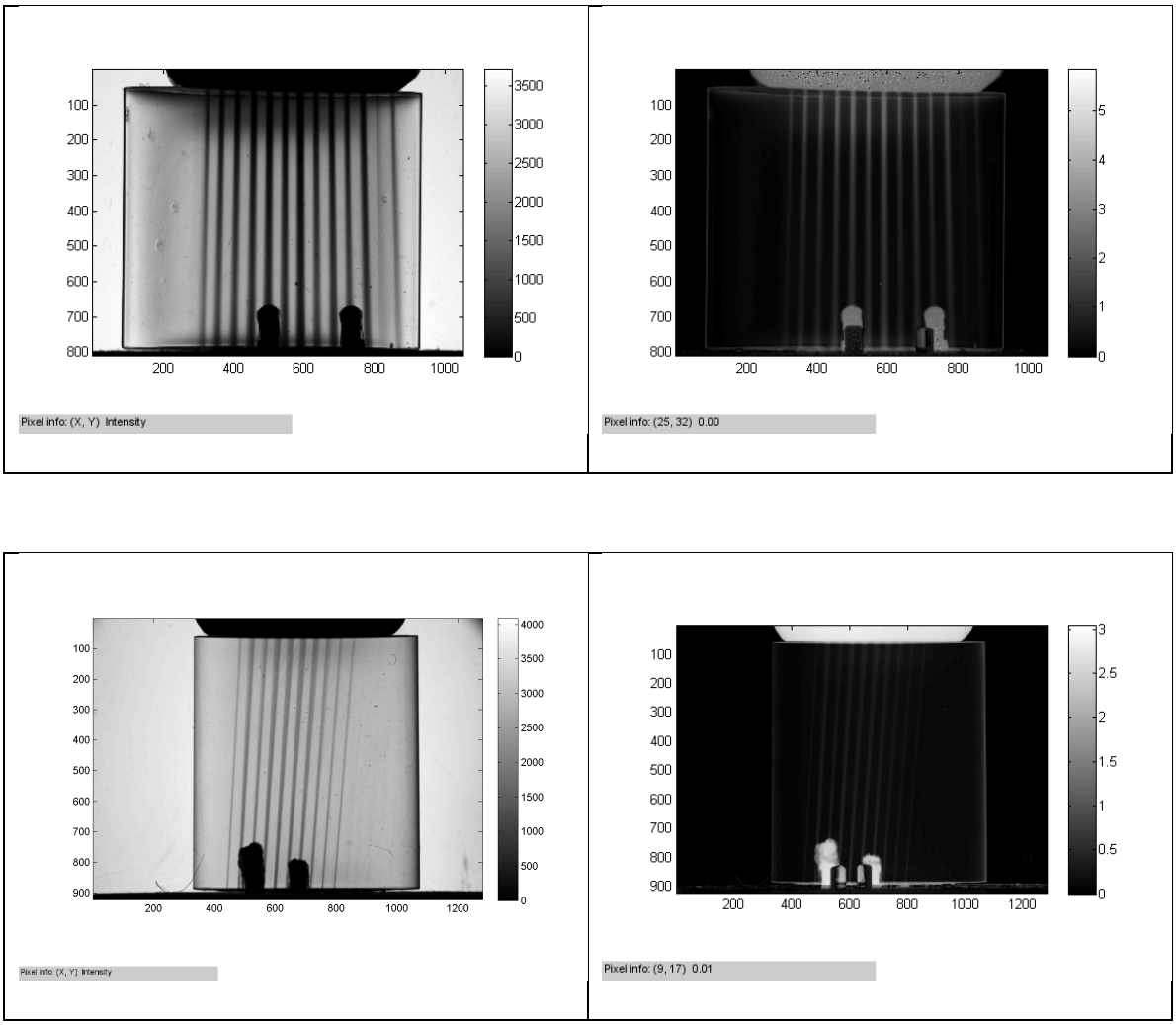

Figure 21 Count Image (left) and OD Image (right) from multi-beam irradiation. (From the most attenuated view) Top row: UNC_D; Bottom row: UNC_E.

For convenience, the thirteen beams were labeled as figure 22:

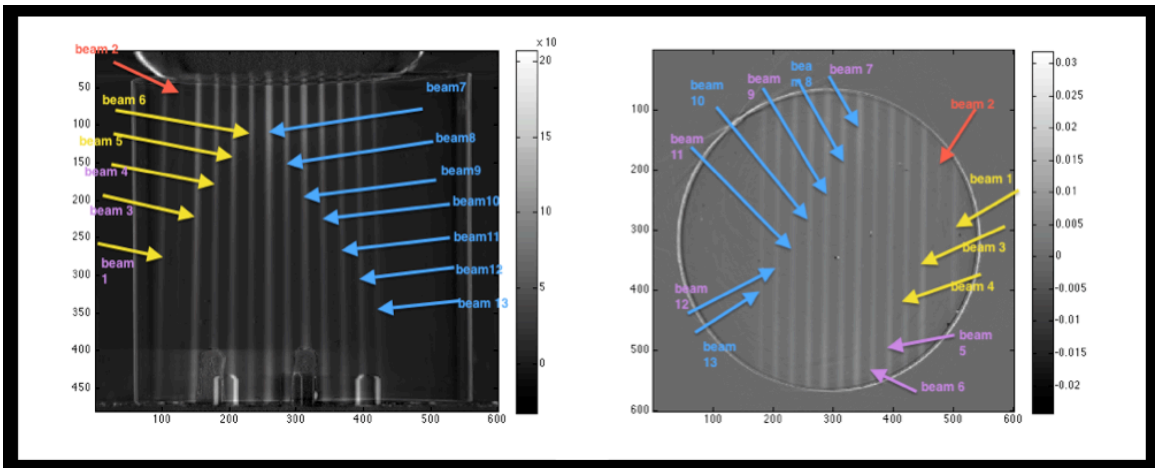

Figure 22 Reconstructed OD images show how beams were labeled.

Note: In the following analysis, a 100 pixel (5 mm) central section of the OD has been averaged and saved as a 2D matrix, which can be used to analyze the data.

3.3.1 Percentage-Depth-Dose (PDD) for Multi-beam Irradiation

As can be seen from figure 22, all of the thirteen beams' intensities and beam widths vary largely, which indicates that the dose delivery between these thirteen beams are nonuniform(which contradicted with what was intended). Therefore, for data analysis, we only choose the 3 beams at the center (beam 7, 8, 9) to analyze. Figure 23 shows the OD drop as a function of depth of beam 7, 8, 9.

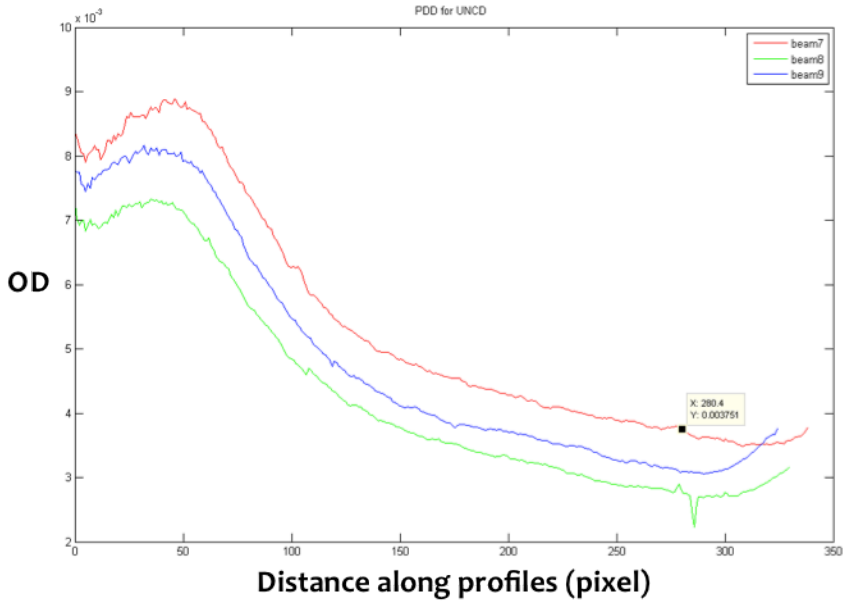

Figure 23 PDD for Beam 7, 8, 9.

Table 6 PDD Comparison for Multi-beam Irradiation. (PDD was normalized to its dmax~2mm)

Dosimeter	Entrance dose	PDD falls off to (%) at a depth of 14mm (mean of 3 beams)	PDD falls off to (%) at a depth of 14mm (sigma of 3 beams)
UNC_D	32 Gy	39.5%	2.5%

3.3.2 Beam Width (FWHM) for Multi-beam Irradiation

Line profiles (shown in figure 24) were taken horizontally accross the selected three beams (beam7, 8, 9) on the averaged reconstructed slice.

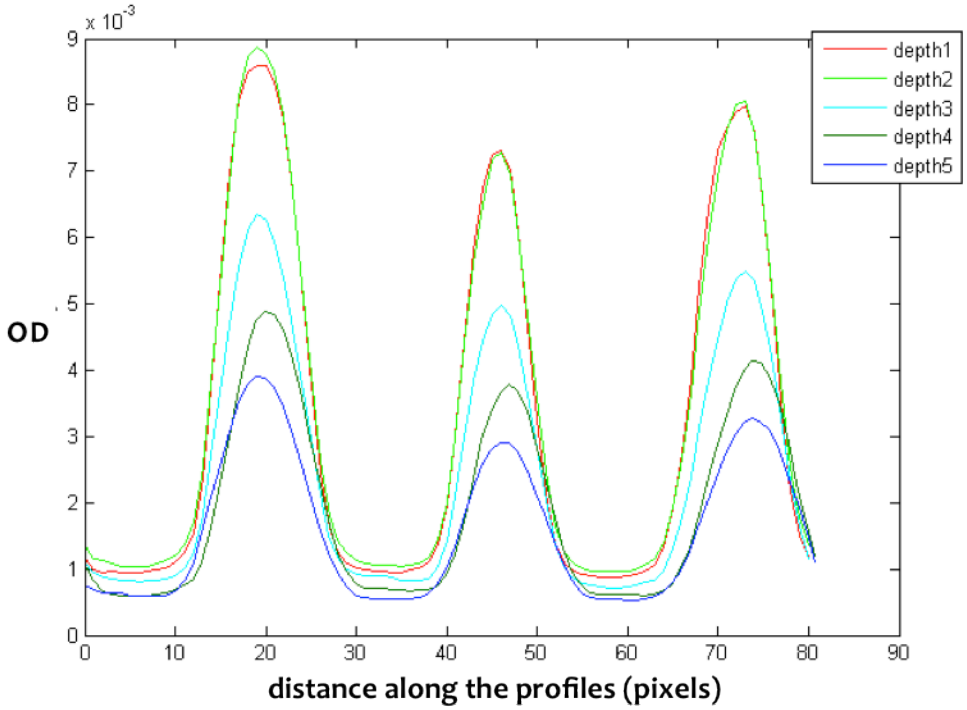

Figure 24 Beam widths for beam 7,8,9 (from left to right is beam 7, 8, 9).

Table 7 Summary of FWHM for UNC_D

	Beam 7 (averaged from 5 depth)	Beam 8(averaged from 5 depth)	Beam 9(averaged from 5 depth)
FWHM	549.2 um	441.2 um	499.5 um
Average FWHM across three beams	496.5 um (mean) 54.1 um (Sigma)		

3.3.3 Peak-Valley-Dose-Ratio (PVDR) for Multi-beam Irradiation

At the same depth, all beams' PVDRs are different (all the valley values are similar but not the peak values). Between different depth, PVDRs of a particular beam

(for example the center beam: beam 7) seem that do not vary much (2.3 for depth 1 and 5.7 for depth 6). Because of the same reason (the variation for thirteen beams is too large), only 3 beams (beam 7, 8, 9) were analyzed. The results are summarized in table 8.

Table 8 PVDR Comparison for Multi-beam Irradiation.

Dosimeter	Entrance dose	Average PVDR at depth 3mm	Average PVDR at depth 14mm
UNC_D	32 Gy	8.0	6.1

3.4 Three Strips MRT Irradiation Experiment

From the reconstruction GUI, several post irradiation images (with the most attenuated beam direction) were pulled out as well as their OD images. As can be seen in figure 25, there were three strips delivered with a fixed beam angle. As seen that there are not much variation between beam width/beam spacing in different depth and there is not much divergence problem, it is possible to analyze the dosimetric data automatically by programming a code in MATLAB. Preliminary analysis of microbeam characteristics was performed on a ROI averaged across the central 10 mm of the dosimeter.

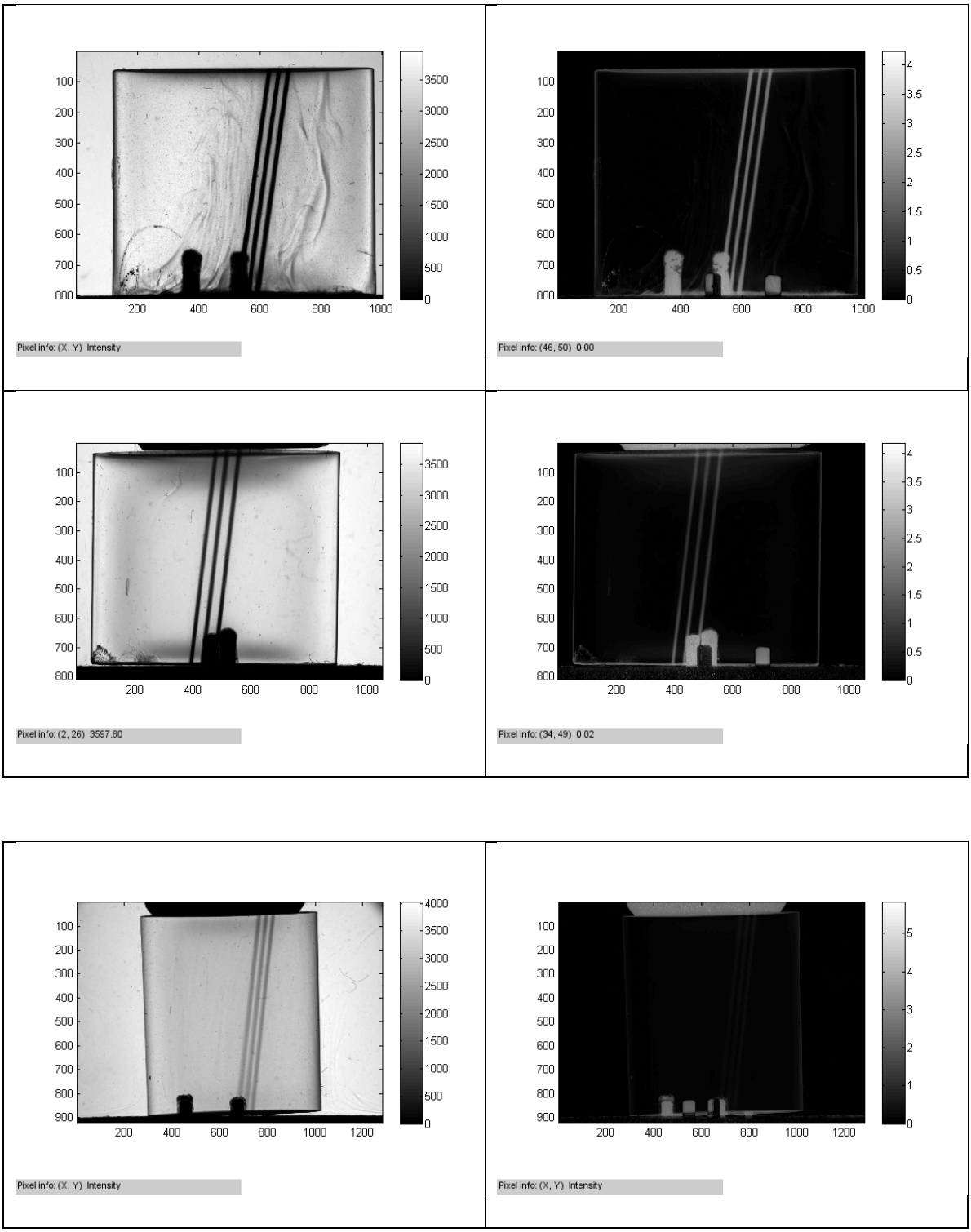

Figure 25 Count Image (left) and OD Image (right) from 3 strips irradiation (from the most attenuated view). Top row: UNC_A; Middle row: UNC_C; Bottom row:

UNC_F. Note that the count image in UNC_A shows an artifact of schleifring bands, which could be caused by the imperfect smooth surface of the dosimeter and different fluids not distribute evenly.

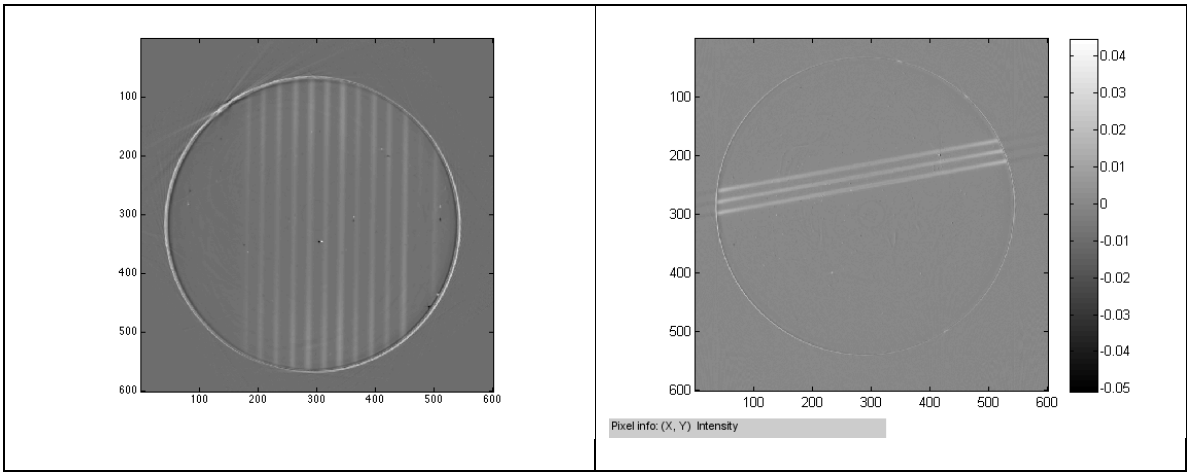

Figure 26 Axial Views of Dosimeters in a reconstructed OD image slice (center slice of the reconstructed matrix). Multi-beam is on the left and three strips is on the right.

For convenient the beam was labeled as figure 27:

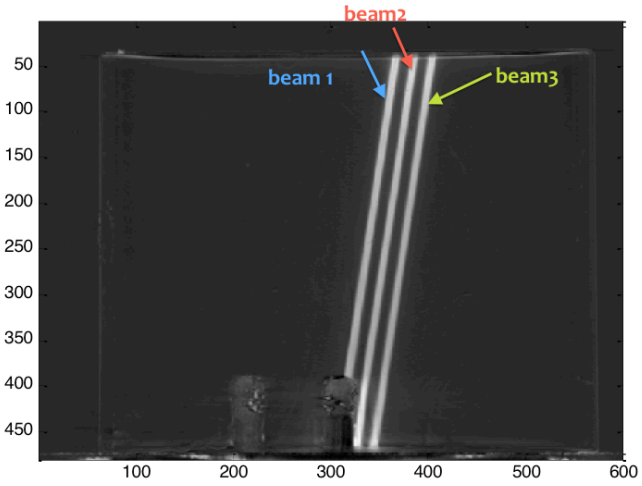

Figure 27 Reconstructed image shows how beams labeled in three strips irradiation.

Note: In the following analysis, a 200 pixel (10 mm) central section of the OD has been

averaged and saved as a 2D matrix, which can be used to analyze the data.

3.4.1 Percentage-Depth-Dose (PDD) for Three Strips Irradiation

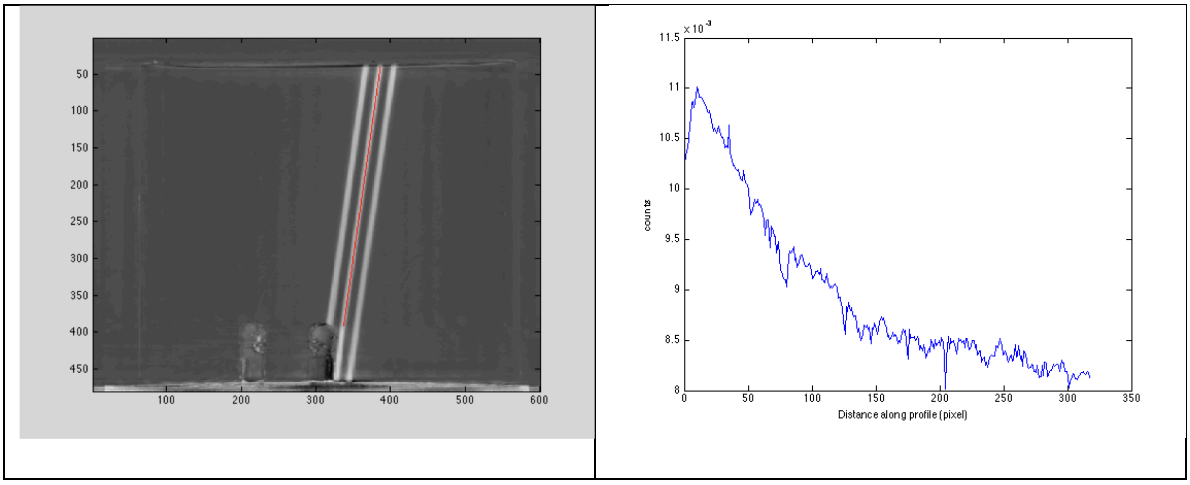

Figure 28 Line Profile along the Depth of Dose from a reconstructed image slice. Use UNC_A as an example in this figure.

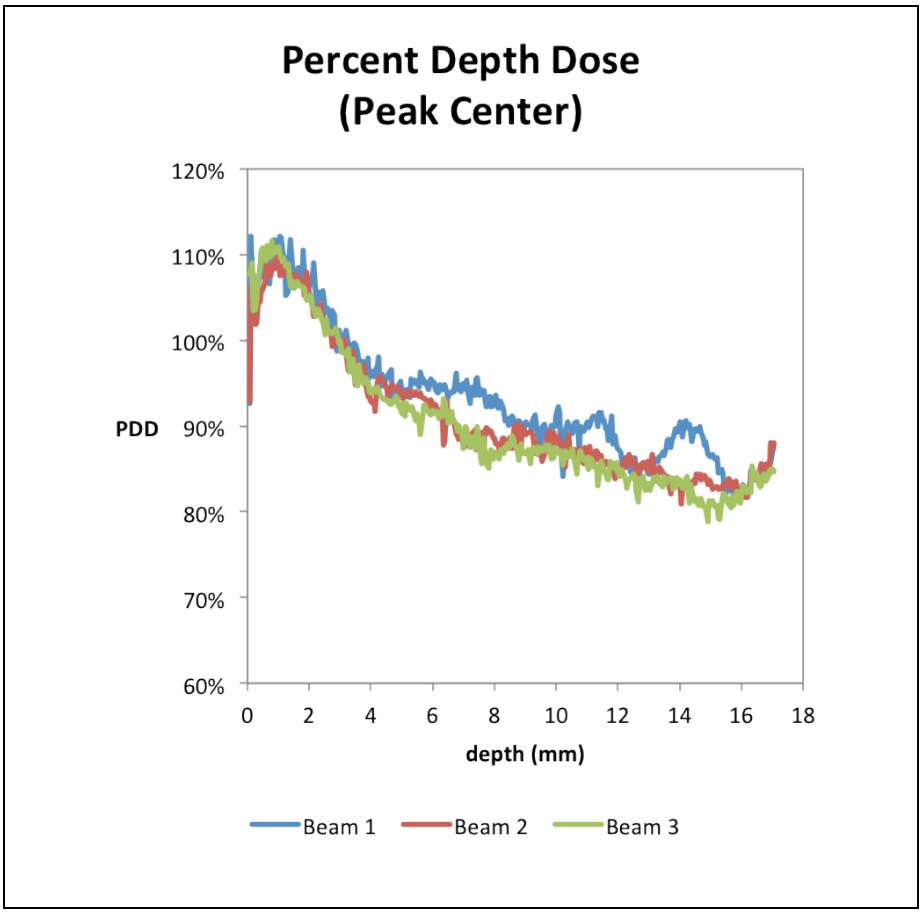

Figure 29 PDDs in UNC_A (This figure is from Titania Juang).

UNC_C dosimeter was also obtained but unexpected rising was shown at the end of the curve.

Table 9 PDD Comparison for three strips Irradiation. PDD was normalized to its dmax~3mm.)

Dosimeter	Norminal dose	PDD falls off to (%) at a depth of 14mm (mean of 3 beams)	PDD falls off to (%) at a depth of 14mm (sigma of 3 beams)
UNC_A	32 Gy	86.5%	5.7%
UNC_C	32 Gy	102.1%	9.1%

3.4.2 Beam Width (FWHM) for Three Strips Irradiation

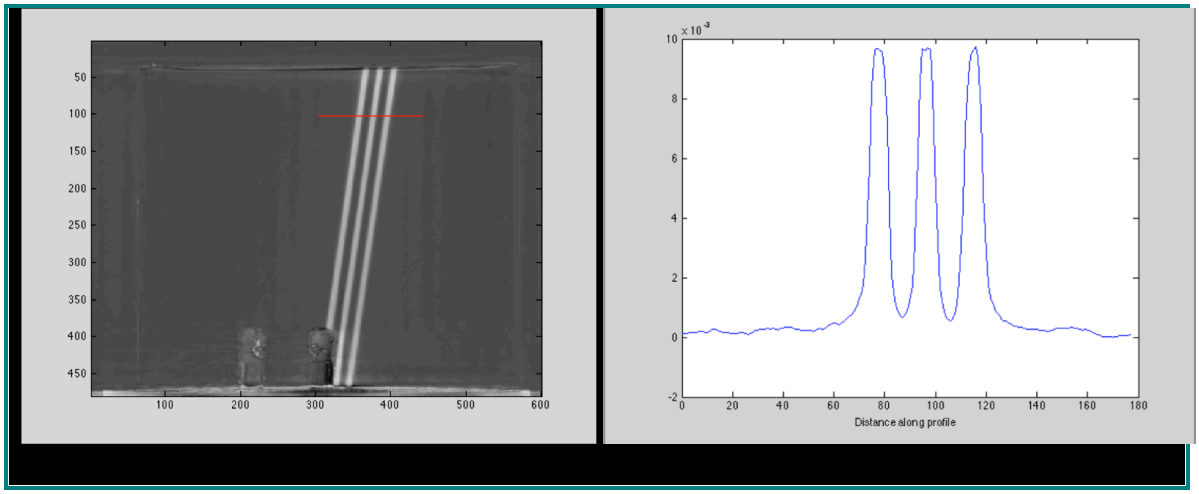

Figure 30 Beam Profiles Crossing the Three Strips on a Certain Depth in a reconstructed image slice. Use UNC_A as an example in this figure.

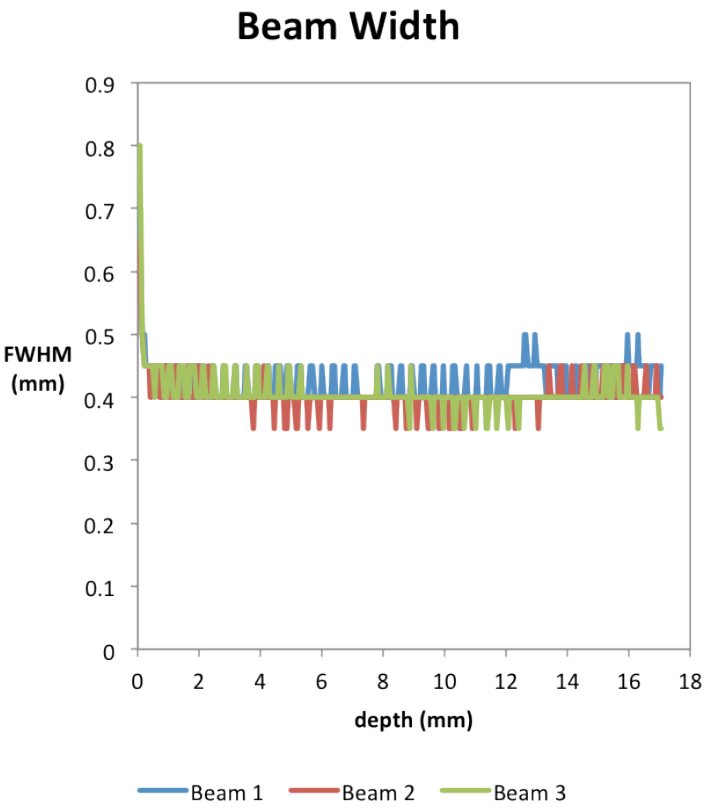

Figure 31 Beam Width for UNC_A (This figure is contributed by Titania Juang). It shows FWHM for all three beams as a function of depth.

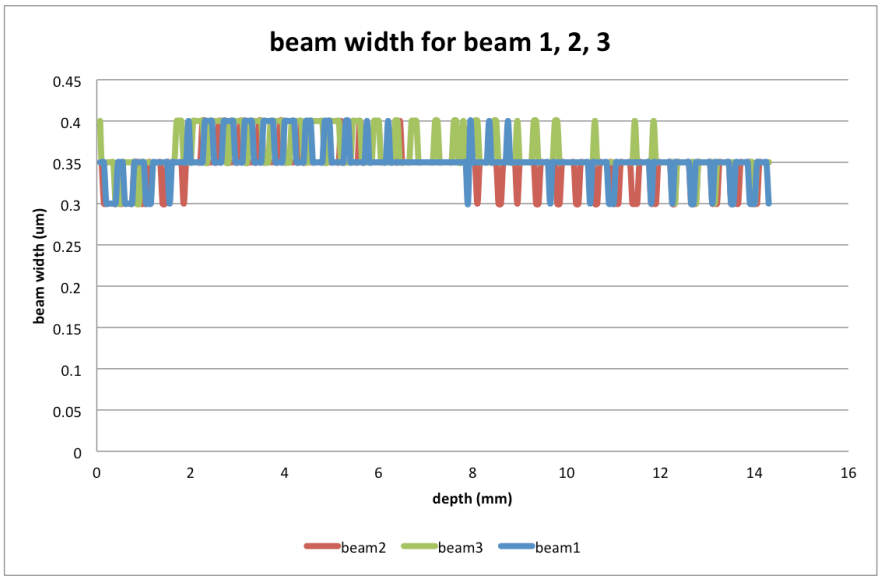

Figure 32 Beam Widths for UNC_C.

Table 10 FWHM Comparison for three strips Irradiation.

Dosimeter	Entrance dose	Average FWHM (between depth of 3mm~14mm) accorss three beams	
		mean	Std (sigma σ)
UNC_A	32 Gy	405.3um	13.2um
UNC_C	32 Gy	350.6um	19.5um

3.4.3 Peak-Valley-Dose-Ratio (PVDR) for Three Strips Irradiation

PVDR was calculated from averaging of maximum values of each peak divided by average of minimum values of each valley. PVDR was plotted as a function of depth for UNC_A(shown in figure 33). Depth was measured along the beam path.

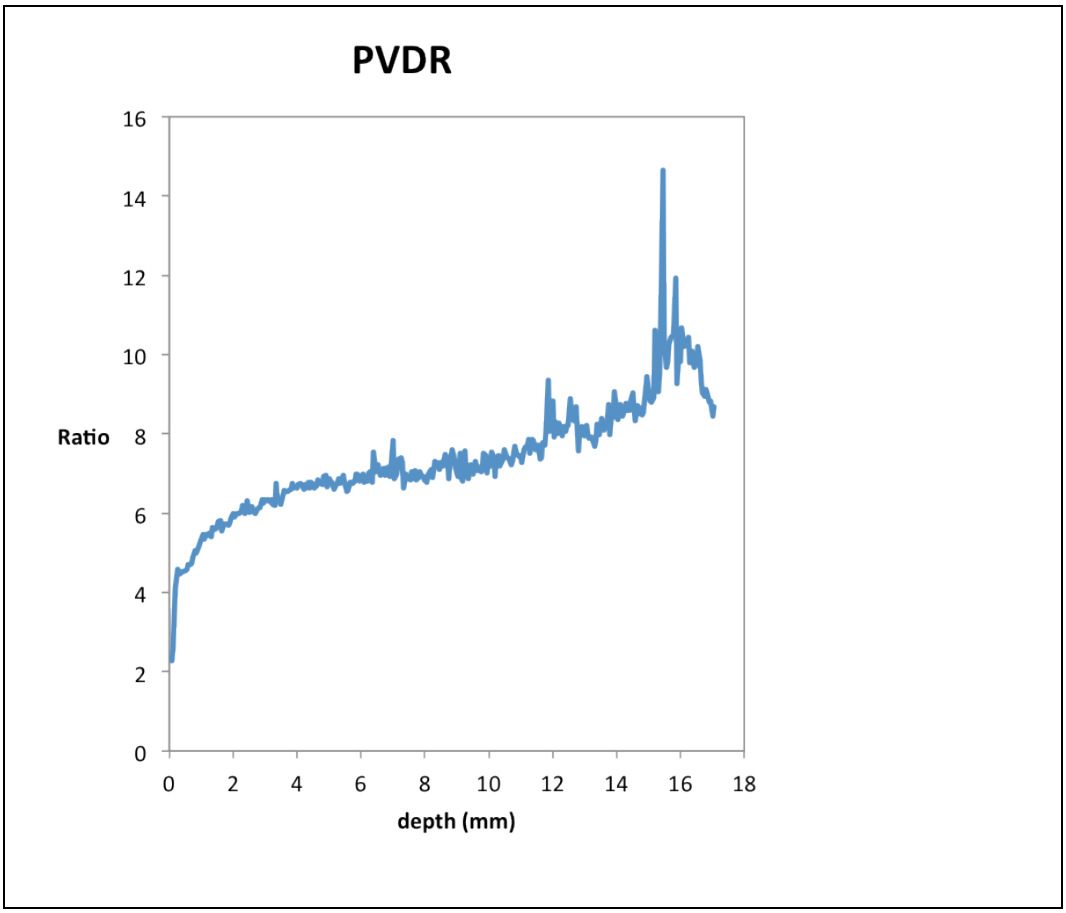

Figure 33 PVDR for UNC_A. (This figure is contributed with assistance from Titania Juang)

PVDRs were also obtained for UNC_C dosimeter. However, some unexpected negative values as well as very large values were shown. Further investigation about the reasons will be provided in the future.

Table 11 PVDR Comparison for three strips Irradiation.

Dosimeter	Entrance dose	Average PVDR at depth 3mm	Average PVDR at depth 14mm
UNC_A	32 Gy	6.3	8.6
UNC_C	32 Gy	21.9	60.4

3.5 Gafchromic EBT2 Film Verification Test

3.5.1 Calibration Curve

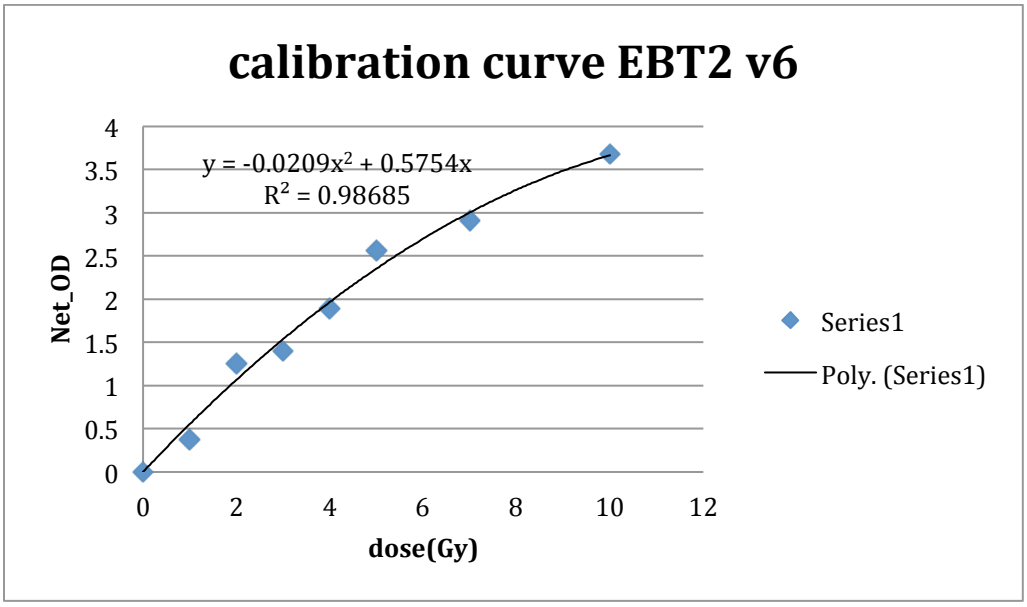

Figure 34 Calibration Curve for EBT2 film. A second order polynomial function was selected to fit the data.

3.5.2 Experimental Films (Three Angled Beams/Multi-beam) Data Analysis

The analysis data will be presented in the future.

3.6 UNC independent (Three Angled Beams/Multi-beam) dosimetry measurements

The performance of CNT MRT system was also tested by UNC group. The dosimetric measurements were based on both Gafchromic EBT2 film and nanocrystal dosimeter. According to their report, the results from film measurements and nanocrystal dosimeter measurements were very consistent with each other. A

comparison between the results of UNC and that of Duke is shown in table 12. Only beams' width/spacing and PVDRs were reported in table 12 because only 2D measurements were performed UNC side.

Table 12 Compare dosimetry measurements' (UNC_C) results from UNC and Duke.

	Beam width	PVDR
UNC	350	11.5
Duke	350.5	21.9-60.4
%Difference	0.04%	15.6%-34.0%

4. Discussion

4.1 Compare with Traditional RT

A limitation of MRT is the inability to use megavoltage photon energy. Since the megavoltage beams possess greater penetration depth and the build up effect could essentially spear the skin tissue. Because of the constraints mentioned in the section 1.1.1, megavoltage could not be used in the MRT study, thus MRT loses all the benefits introduced by megavoltage in radiation therapy.

Secondly, problems such as beam divergence and motion can be more frequently encountered and less tolerant than in traditional RT because of the small field involved. Therefore, the higher accuracy and thus more complicated collimating system and immobilization system are in urgent need for MRT development.

4.2 Compare Compact CNT MRT system and Multi-beam MRT system

To a large extend, the results showed that many advantageous aspects of the CNT MRT system than the Multi-beam MRT (table 13): more build-up regions, stronger penetration, smaller and more stabilized beam width, more consistent PVDR and etc.

Table 13 Comparison of compact CNT MRT and Multi-beam MRT dosimetric performance

	Maximum depth (dmax)	Beam width achievable	PDD drop percentage at 14mm	PVDR
CNT-MRT	3 mm	350~405 um	86.5%	6.3~8.6
Multi-beam RT	2 mm	496 um	39.5%	6.1~8.0

Especially, by comparing projection taken from three strips experiment and multi-beam experiment, the most challenging issue in MRT, which is the beams diverging, had been excellently addressed and improved in CNT MRT development. However, more efforts need to be carried out to improve the penetration of the beam, increase the PVDR and etc.

Although there is no prior MRT work has been done by using this particular device from the UNC side, I assume the method to estimate the beam width and beam spacing would be based on the following method: as illustrated from figure 35, add the total thickness of the bricks and subtract from the total length of the groove; use this value divided by number of spacing to acquire the average separation in between bricks.

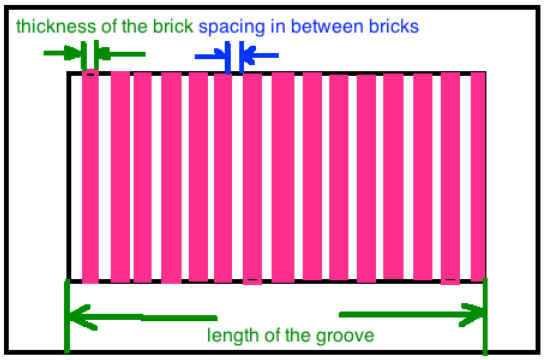

Figure 35 Illustrations of Estimating Beam Width and Spacing.

As can be seen this is a very rough method to determine the spacing and beam width due to the fact that there is no digital readout for this particular MRT device.

4.3 Compare with UNC group independent dosimetry measurements (beams' width/spacing and PVDRs)

Comparing UNC's results with our results, the beam width measurements are very consistent with each other (beam width: within 0.04% difference (shown in table 12)). However, a large difference can be seen in PVDR measurements (PVDR: 15.6%-34.0% difference (shown in table 12)).

4.4 Artifacts

Some of the results above already indicated some of the artifacts encountered in this study such as donut/ring artifact, stray light scattering artifact, fluid related artifact and etc. These artifacts are largely degraded the image quality and distorted dosimetry

information. Some of the proposed correcting/ reducing artifacts methods are presented here for each section.

4.4.1 Donut Artifact

Donut artifact (shown in figure 36) is very common during the reconstruction process. It resulted in an inappropriate Center of Rotation choosing.

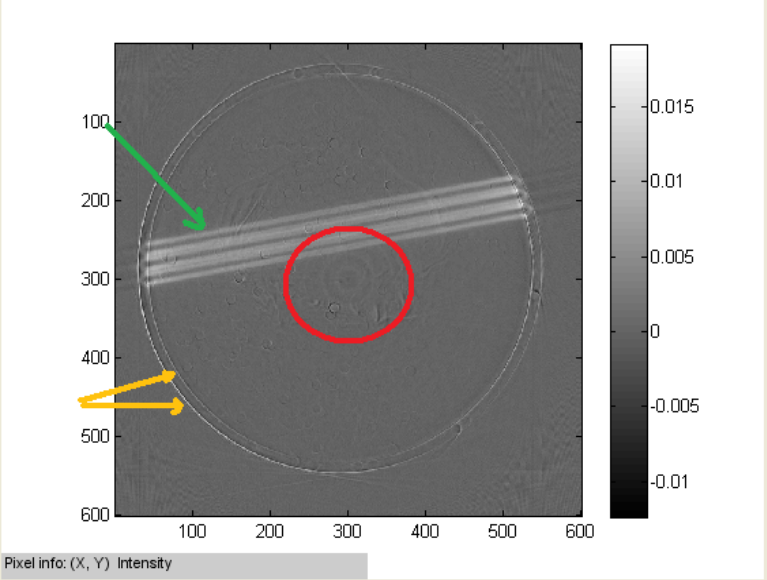

Figure 36 Artifacts due to the inappropriate Center Of Rotation (COR). Axial view of a dosimeter shows three strips across the center. Red circle shows the "donut"; Green arrow indicates the three strips blurred out to four; yellow arrows shows the "ring".

So, using the methods mentioned in 2.2.3.2 (5) to choose the most appropriate COR has significant meaning.

4.4.2 Stray Light Artifact

This has been illustrated in the methods and results section. It is listed here for completion purpose.

4.4.3 Imperfect Registration of Pre-scan and Post-scan

Usually, the imperfection surface can be seen from the above figure will be automatically corrected by taking the pre-scan and post-scan. However, the perfect registration cannot be easily achieved because of the following several types of causes. Usually, these artifacts can be easily detected as “rings” on the outside surface of the dosimeter, or can be detected from discovering a pair of dark spike and a white spike on the reconstructed axial dosimeter image as seen figure 37.

Due to the time gap between the pre-scan and post-scan, the system can be disturbed by different factors. It is best to arrange the pre-scan and post-scan within one day that can keep the system less disturbed. If the dosimeter is hugely affected and ring artifact is sever, a manually registration is required.

Another cause of ring artifact is because that rotations for pre-scan and post-scan are not initialized in the same position. For instance, if the rotation was abrupt and restarted, the system will still precede 720 steps without going back to the same starting position as the pre-scan. In this case, a change order of the step numbers is required to act.

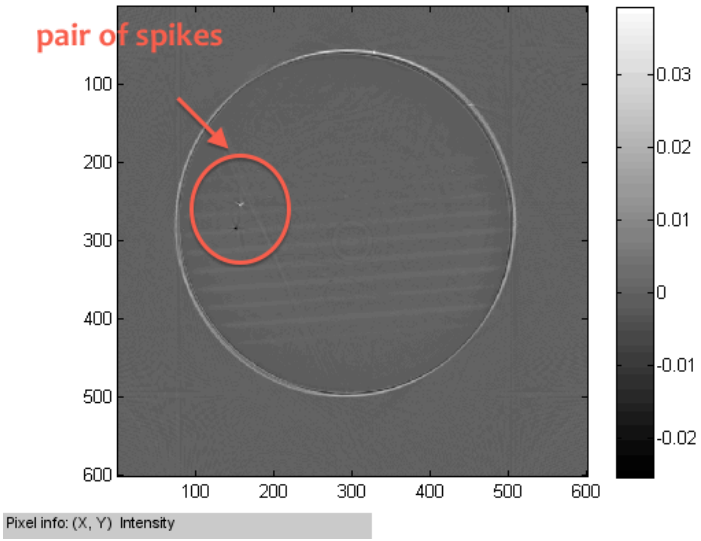

Figure 37 "Pair of Spikes".

5. Conclusions

MRT dosimetry is extremely challenging due to the utilization of ultra-small field sizes and lower energy beams. The prototype ultra-high resolution optical-CT 3D dosimetry system introduced here, showed strong potential for uniquely comprehensive verification of the MRT beams but to achieve high resolution 3D dosimetry requires exceptionally careful procedures. Pervious effort on optimizing fluid matching, standardize the operating procedures, improving the precision of dosimeter mounting and motion, correcting stray-light artifacts has shown promising in improving the capacity of characterizing microscopic radiation beams.

6. Future Work

For the next step, 2D dosimetry analysis needs to be done to verify the accuracy of 3D analysis. Noise need to be filtered out of the UNC_E and UNC_F data. In a long

run, future work on the MRT development side would involve developing more effective delivering system, treatment planning systems and Quality Assurance (QA) protocols and confirming the effectiveness of the MRT on small animal irradiation experiments. On our side, optimizing the mechanical components, developing reproducible procedures for scanning/artifact correction and exploring more efficient analyzing tools for MRT study will be the next action.

Appendix A

EBT2 Film Calibration Procedure:

1. Load .TIF files into MATLAB workspace by using imread() function.
2. Separate RGB channels, use red channel ONLY.
3. Extract all the needed intensity values (use mean value) from a defined center ROI (Region Of Interest) area (616 in area). Use ImageJ software tool: Analyze>measurement.

   (An alternative method is to use MATLAB function imfreehand() to choose a Region of Interest (ROI). Then, the mean value will be taken of the ROI region for each piece of film.
4. Export all the intensity values into the excel worksheet. Includes post_dark_red, pre_dark_red, post_red, pre_red.
5. Calculate Net OD (the change of the optical density), the derivations are as follows:

$$OD = A / L$$

$$A = -\log_{10}\left(\frac{I_1}{I_0}\right)$$

$$OD_{post} = -\frac{1}{L}\log_{10}\left(\frac{I_1}{I_0}\right)_{post} = -\frac{1}{L}\log_{10}\left(\frac{I_{post} - I_{post\_dark}}{I_{post\_flood}}\right)$$

$$OD_{pre} = -\frac{1}{L}\log_{10}\left(\frac{I_1}{I_0}\right)_{pre} = -\frac{1}{L}\log_{10}\left(\frac{I_{pre} - I_{pre\_dark}}{I_{pre\_flood}}\right)$$

$$Net\_OD = OD_{post} - OD_{pre}$$

Note: A is absorbance; L is the voxel length, which is 0.2mm in this case; I_1 is the transmitted light intensity (pre-scan or post-scan) and I_0 is the incident light intensity (pre-flood or post-flood). Here, all the intensity values are from the red channel only. (Since assume the flood will be same in both pre and post scans, the two terms will finally cancel out each other, so there is no need to acquire flood images)

6. Plot Net_OD as a function of dose value. Fit with polynomial second degree.

Appendix B

EBT2 Film Scanning Procedure:

Before irradiation:

1. Block the whole film scan region and take three dark images for prescan.

(Choose all the parameters according to the screen capture shown in figure 38)

2. Cut the film into small pieces. Label all the pieces with black ink on the right corner.
3. Place all of the pieces on the scanner with the labeled side on top and block all other areas within the film scanning area.
4. Carefully tap and mark the edge of the films.

(Choose all the parameters according to the screen capture shown in figure 38)

5. Take three pre-scans and save them as .TIF file.
6. Take off the films but leave the blocked area still blocked.

After Irradiation:

1. Place the post-scan on the scanner (figure 39). Make sure place them at the exact places as the prescans by matching up with the edges. Also make sure the side is the same as before.
2. Do the three post-scan and save it as the .TIF file.

3. Take off the film and block the whole area for dark scanning. Take three dark images for post-scan image.

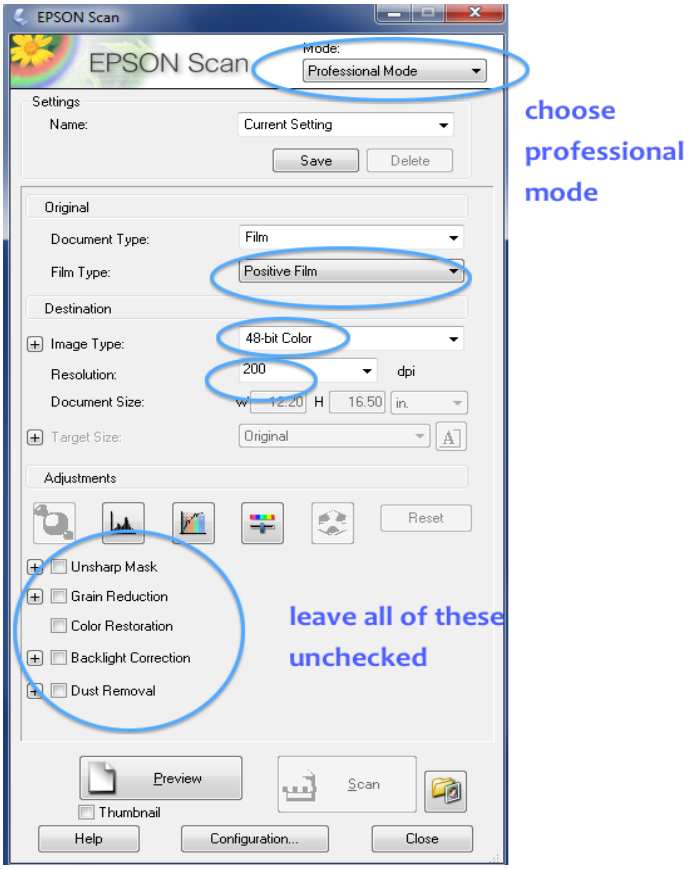

Figure 38 Choose Scanning Parameters.

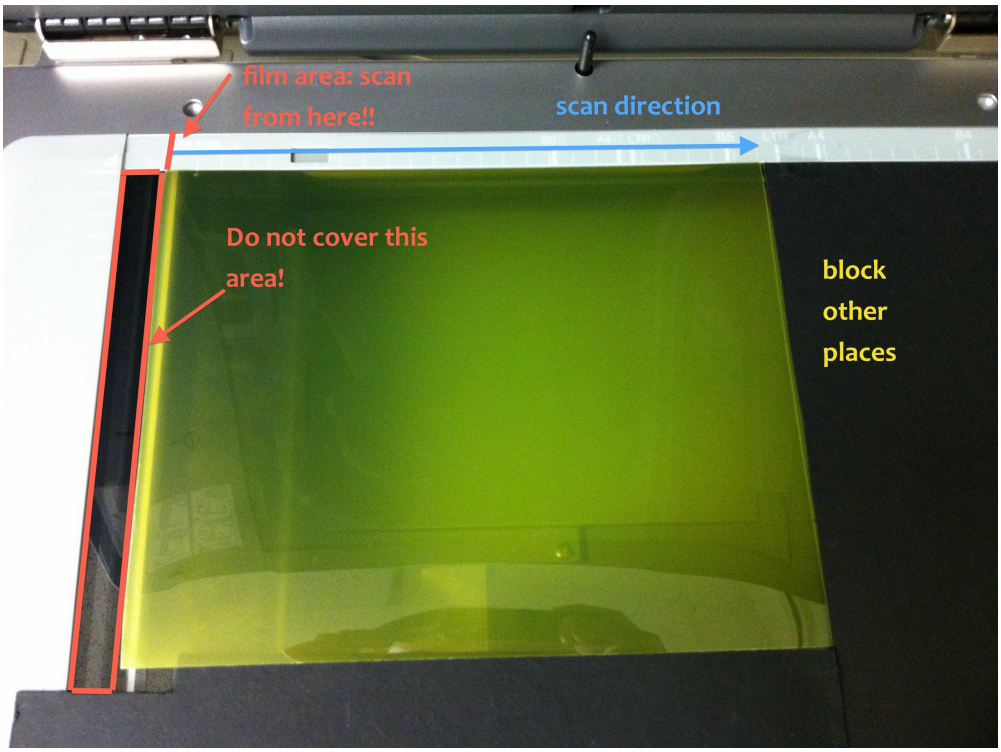

Figure 39 Positioning Film on the Scanner. Place the film on the "film scanning area". Block other places using black paper.

References

R. Siegel, J. Ma, Z. Zou, and A. Jemal, CA Cancer J Clin **64** (1), 9 (2014).

Jr. Michael John Hadsell, UNC-Chapel Hill PhD dissertation (2013).

J. C. Crosbie, R. L. Anderson, K. Rothkamm, C. M. Restall, L. Cann, S. Ruwanpura, S. Meachem, N. Yagi, I. Svalbe, R. A. Lewis, B. R. Williams, and P. A. Rogers, Int J Radiat Oncol Biol Phys **77** (3), 886 (2010).

A. Bouchet, B. Lemasson, G. Le Duc, C. Maisin, E. Bräuer-Krisch, E. A. Siegbahn, L. Renaud, E. Khalil, C. Rémy, and C. Poillot, International Journal of Radiation Oncology* Biology* Physics **78** (5), 1503 (2010).

M. Hadsell, J. Zhang, P. Laganis, F. Sprenger, J. Shan, L. Zhang, L. Burk, H. Yuan, S. Chang, J. Lu, and O. Zhou, Appl Phys Lett **103** (18), 183505 (2013).

M. Alqathami, J. Adamovics, R. Benning, and A. Blencowe, Journal of Physics: Conference Series **444**, 012034 (2013).

M. Oldham, Advances in Medical Physics. (Chapter x) Ed. by D. Godfrey. (2014 in press).

T. Juang, J. Newton, M. Niebanck, R. Benning, J. Adamovics, and M. Oldham, J Phys Conf Ser **444**, 012029 (2013).

T. Gorjiara, A. Kacperek, Z. Kuncic, C. Baldock, and S. Doran, Journal of Physics: Conference Series **444**, 012058 (2013).

A. Thomas, J. Newton, and M. Oldham, Phys Med Biol **56** (14), 4433 (2011).

N. Annabell, N. Yagi, K. Umetani, C. Wong, and M. Geso, J Synchrotron Radiat **19** (Pt 3), 332 (2012).